Quantifying Entrainment in the Planetary Boundary Layer Morning Transition

Samuel J. Kimball

A Thesis submitted in partial fulfillment of
the requirements for the degree of

Master of Science
(Atmospheric and Oceanic Sciences)

at the
UNIVERSITY OF WISCONSIN-MADISON
May 2026

Abstract

The morning transition of the Planetary Boundary Layer (PBL) plays a critical role in controlling the evolution of heat, moisture, and depth of this important layer. Entrainment of air from the free troposphere is an important forcing on this transition, yet its role is not fully understood due to limitations in observing it. A recent advancement in the ability to measure horizontal advection has allowed a pathway to quantify entrainment through the closure of heat and moisture budgets using mixing diagrams constructed from remote sensing observations. This novel budget closure method is tested and applied to the morning transition using ground-based remote sensing instruments at the Department of Energy Atmospheric Radiation Measurement Southern Great Plains (SGP) site. The result is a dataset of 61 clear air entrainment cases over SGP from 2018-2019 used to understand the strength and variability of entrainment in the morning transition and to analyze its relationship to land and synoptic-scale atmospheric conditions. The results show how the water vapor component energetically dominates the variability in morning entrainment, with weaker and less variable forcing in conditions of high surface pressure and anti-cyclonic winds. The analysis demonstrates how entrainment is governed by a combination of vertical entrainment zone gradients, surface fluxes, surface conditions, and processes unique to the morning transition. The resulting observational dataset provides a foundation for testing PBL entrainment theory and furthering our understanding of land-atmosphere interactions in the PBL morning transition.

Acknowledgements

I would like to acknowledge the Department of Energy (DOE) Atmospheric Systems Research (ASR) program for funding this work and making it possible. This type of scientific discovery can only be completed with the wealth of instruments and observation systems deployed at Atmospheric Radiation Measurement (ARM) sites provided by the DOE.

Thank you to my research advisor Dr. Tim Wagner, who's clear ambition and fascination for science kept me motivated to complete this work. Tim played a strong role in developing me as a scientist, and I will forever be grateful for his influence.

I would also like to thank my AOS academic adviser Dr. Angela Rowe. She contributed much of her time to ensure the success of this work. I left every review session with her more motivated and excited to produce a scientific story.

Finally, I would like to thank all my peers in AOS, my friends both at Wisconsin and beyond, and my family for supporting me along the way to completing this project.

Contents

List of Figures

List of Tables

Abbreviations

PBL	Planetary Boundary Layer
CBL	Convective Boundary Layer
SBL	Stable Boundary Layer
RL	Residual Layer
EZ	Entrainment Zone
LLJ	Low-Level Jet
TKE	Turbulent Kinetic Energy
MSLP	Mean Sea Level Pressure
RH	Relative Humidity
AOD	Aerosol Optical Depth
SOM	Self-Organizing Map
BMU	Best Matching Unit
LES	Large-Eddy Simulation
AERI	Atmospheric Emitted Radiance Interferometer
TROPoe	Tropospheric Remotely Observed Profiling via Optimal Estimation
ERA5	ECMWF Reanalysis Version 5
WRF	Weather Research and Forecasting Model
RRTM	Rapid Radiative Transfer Model
ENSO	El Niño–Southern Oscillation
NWP	Numerical Weather Prediction

Chapter 1

Introduction

1.1 The Planetary Boundary Layer in Transitions

The planetary boundary layer (PBL) forms the lowest part of the atmosphere where it is directly shaped by interactions with Earth's surface. It is the primary zone where turbulent exchange of momentum, heat, and moisture occurs between the land or ocean and the free troposphere, and thus where land-atmosphere interactions exert their strongest influence on atmospheric structure. Most human activity takes place within this shallow layer, therefore the PBL is also where interactions between people and the atmosphere occur, such as air quality issues, weather hazards, and human-impacting climate processes (Stull 1988). It is a frequently changing layer, with distinctly different structure throughout the diurnal cycle. The daytime boundary layer is often referred to as the convective boundary layer (CBL), and is characterized by having a deep, well-mixed layer formed by buoyant turbulence from surface heating. Potential temperature and water vapor mixing ratio are nearly uniform with height in the mixed layer (Holtslag et al. 1986; Stull 1988), depicted in Fig. 1.1. The daytime CBL is capped by the entrainment zone, which is a thin but crucial layer with sharp warming and drying vertical gradients, causing warm, dry air from the free troposphere to mix into the PBL, controlling its growth and properties (Gryning and Batchvarova, 1994). After sunset, rapid radiative cooling near the surface compared to slower cooling aloft increases static stability, suppresses turbulence, and traps cooler air near the ground. This forms the shallow, weakly turbulent, nocturnal stable boundary layer (SBL) (Stull 1988), and through this SBL formation process, the warmer well-mixed air from the daytime CBL can decouple from the nocturnal SBL, creating a nearly adiabatic mixed layer above the SBL, called the residual layer, with a capping inversion above. The residual layer forms overnight and can persist well into the morning. Residual layers may also not be simply the remains of the mixed layer of the previous day at the same location; the residual layer at a certain site may have formed elsewhere and be advected in (Stull 1988; Angevine 2020).

Of particular importance in the overall structure is the height of the PBL. There are many definitions and methods used to obtain PBL height and calculating it is an entire field of research. Thermodynamic methods include the height of the strongest potential temperature gradient, the height where potential temperature increases above the mixed layer value by a threshold, and when the Richardson number crosses a critical value. Turbulence-based methods define it using a minimum turbulent kinetic energy (TKE) threshold or when momentum or heat flux crosses zero. More advanced remote sensing

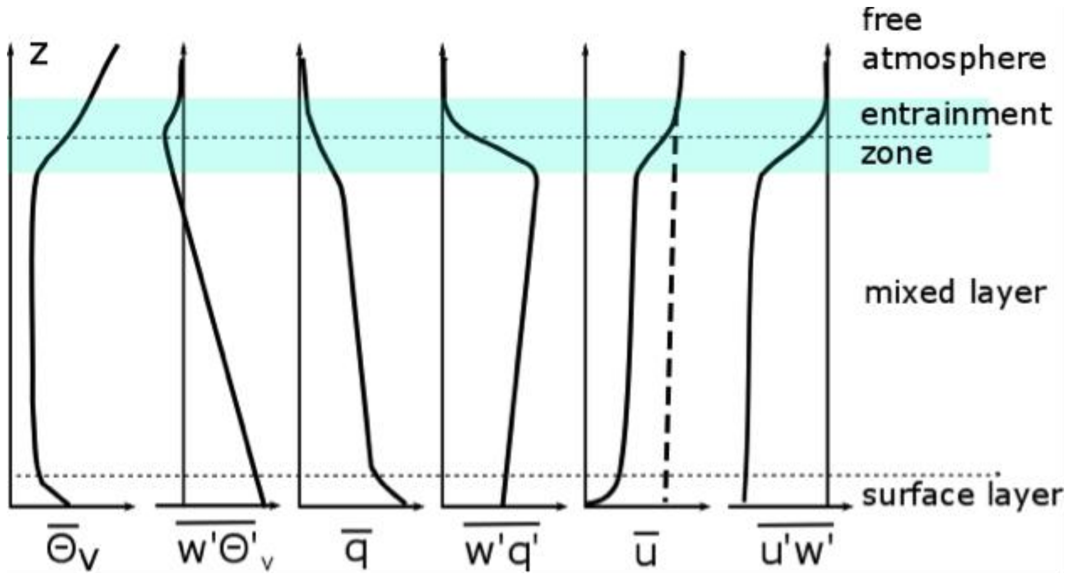

Figure 1.1: (From Tennekes and Driedonks, 1984) Mean values and turbulent vertical fluxes of virtual potential temperature, specific humidity, and horizontal momentum for daytime conditions.

methods take the maximum aerosol backscatter gradient, variance-based lidar detection, and radar refractive index structure parameter (von Engeln and Teixeira 2013, Seibert et al. 2000, Stouffer et al. 2024).

The PBL is generally understood in the two relatively steady states of the daytime CBL and nocturnal SBL throughout the diurnal cycle and have long been well-characterized through observations and modeling (LeMone et al. 2019). However, the transitions between the SBL and CBL in the morning present a greater challenge for understanding due to their more complicated nature. Forcings that are negligible during the relatively steady state periods are more important during the transitions, and process studies need to consider them (Angevine et al. 2020).

The morning transition between the SBL and the fully developed CBL is primarily driven by surface heating caused by the rising sun, and the full transition takes several hours (Angevine 2008). During this transition, solar heating erodes the nocturnal stable layer, and the mixed layer deepens rapidly as the boundary layer height increases and engulfs air aloft typically from residual layers (Stull 1988; Angevine et al. 2001; Blay-Carreras et al. 2014; Angevine et al. 2020). Figure 1.2 shows a visual of the morning transition in potential temperature gradient resulting from a Large Eddy Simulation (LES) model. Observational studies find a quasi-linear increase in mixed layer height during the morning transition, marking the growth of a convective daytime mixed layer to depths of several hundred meters within a few hours (Angevine et al. 2001; Halios and Barlow 2018; Nielson et al. 2022; Henkes et al. 2021). Many processes influence the boundary layer through the morning transition, and the key challenge to understanding is the need to include all relevant forcings. Surface fluxes and entrainment at the boundary layer top play important roles in the growth of the CBL (Angevine et al. 2020). The morning transition is a highly variable process, and its theoretical description and investigation has previously been simplified due to limitations in observations (Fritz et al. 2021).

The morning transition is important for air quality, convective inhibition, climate feedback, and energy. It does so by controlling the depth of the CBL and entrainment zone, resulting in implications for human health and weather forecasts (Crook 1996; Dabberdt et al. 2004; Kalthoff et al. 2011). The morning transition controls the rate of growth and mixing in the lower boundary layer, which greatly affects air quality (Angevine 2001). The top of the PBL confines pollutants and other constituents emitted at the surface, directly affecting air quality and human exposure. This is why PBL height, which rapidly

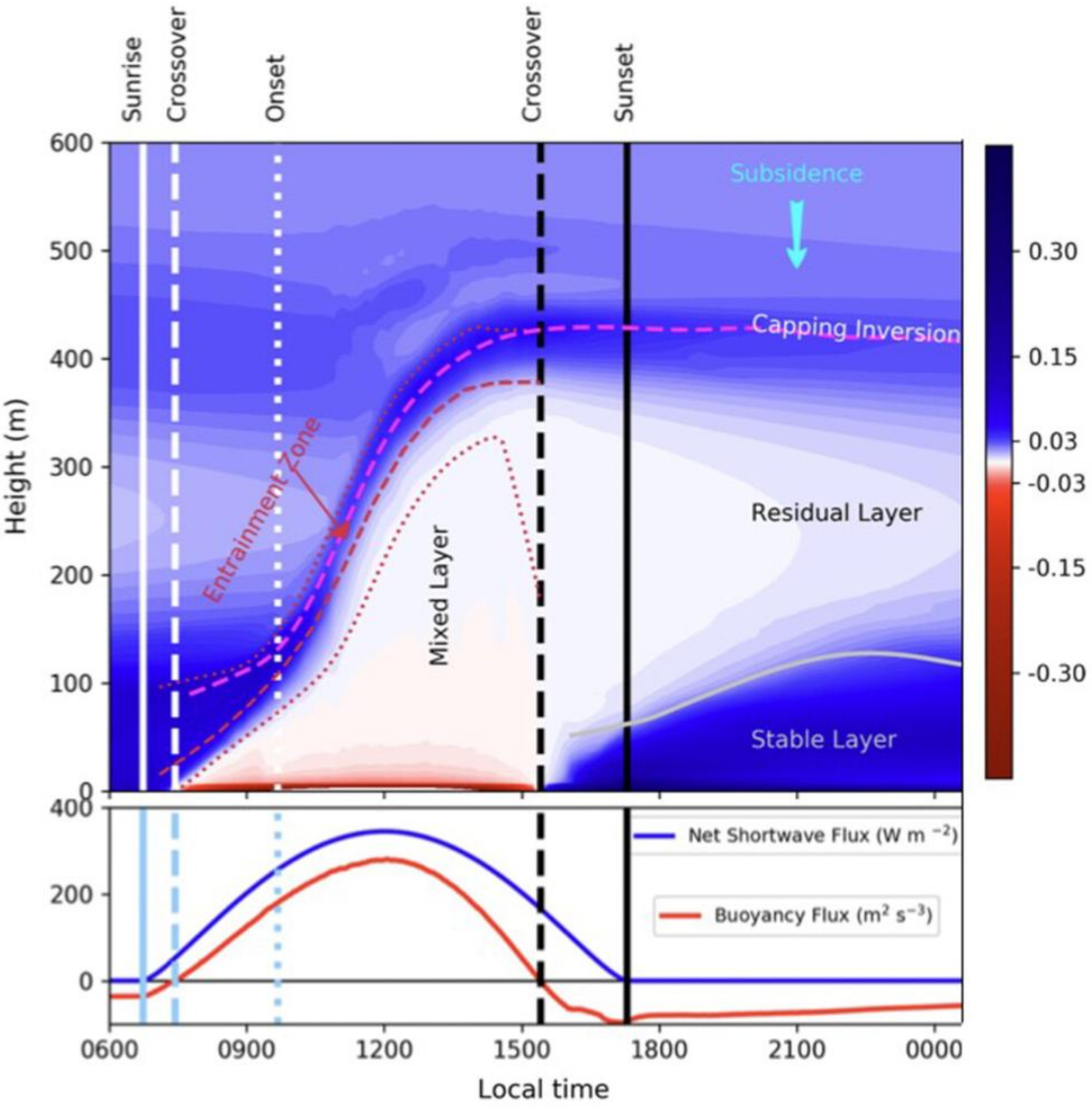

FIGURE 1.2: Angevine et al. (2020): Result of an LES modeling of the morning transition, plotting instantaneous gradient in potential temperature in color.

changes in the morning transition, is an essential parameter in air quality forecasting and dispersion modeling (Lee et al. 2016). A sharp maximum in wind speed occurs just above the nighttime nocturnal inversion, forming a low level jet (LLJ) (Blackadar 1957). Increased wind speed and shear significantly impact wind energy production (Gadde et al. 2021). During the morning transition, erosion of the nocturnal inversion weakens the low-level jet, making the timing and intensity of this transition important for turbine performance (Stull 1988). Henkes et al. (2021) shows how the morning transition is also the critical setup period for deep convection. One of the most important implications of the morning transition is its control on the heat and moisture of the PBL. The heat and moisture feedback systems between the PBL and the surface can amplify severe weather and climate issues, including heat waves and droughts, impacting agriculture and human health (Miralles et al. 2014, 2019; Schumacher et al. 2019; Wakefield et al. 2019; Christian et al. 2020; Benson and Dirmeyer 2021). Along with drought feedback, PBL and surface coupling involving heat and moisture can also lead to extremes in the other direction. It has been shown that excessive surface latent heat fluxes can amplify the re-intensification of tropical cyclones over land and associated excess precipitation (Emanuel et al. 2008; Arndt et al. 2009; Andersen et al. 2013; Wakefield et al. 2021a). Therefore, it is imperative to understand how the morning transition controls the heat and moisture of the PBL in the context of its role in these climate feedback systems.

Because the PBL morning transition has such important implications, it is imperative to represent it well in models. In numerical weather prediction (NWP) models, the boundary layer is modeled throughout its stationary and transition stages through a selected PBL parameterization scheme. The PBL scheme is an important piece of an NWP model and can be a strong source of bias if modeled incorrectly (Banks et al. 2016). Predicting weather and climate depends on reasonably accurate characterization of the vertical exchange of heat, moisture, greenhouse gases, and aerosols between the surface and free atmosphere through the PBL. Modeling this is a challenge because the turbulent processes controlling mixing are complex and vary on a wide range of space and time scales (Seidel et al. 2012). Parameterizations in a chosen PBL scheme can carry bias and affect the quality of the downstream forecast (Cohen et al. 2015). Thus, a thorough understanding of the PBL morning transition is important for improving modeling and extreme weather forecasts.

1.2 Understanding the Morning Transition Through Heat and Moisture Budgets

Because the morning transition strongly controls PBL heat and moisture, understanding the role of each forcing requires analyzing budget terms that diagnose mixed-layer evolution and reveal key physical processes (Stull 1998). These budgets are also critical for quantifying land–atmosphere coupling, estimating surface fluxes at regional scales, and improving coupled model representations (Santanello et al. 2009, 2018). Additionally, they provide a concise framework for evaluating boundary layer models, particularly where entrainment processes are parameterized (Betts et al. 1992).

The mixed layer heat and moisture budgets during the morning transition can be decomposed into contributions from surface fluxes, entrainment, horizontal advection, and radiative heating (Betts 1992). Warming and moistening via sensible and latent heat fluxes, respectively, lead to rapid daytime PBL deepening via convective mixing (Stull 1998). Radiative heating from absorbed downwelling shortwave radiation by aerosols contributes positively to the heat budget but is a relatively minor forcing, especially during the morning transition when low sun angles limit incoming radiation. Advection is the horizontal transport of air with different properties, leading to changes in moisture and temperature. It is an important term for the heat and moisture budgets, and until recently it has been difficult to measure (Angevine 2020). Entrainment is the process of air mixing into the PBL from the free troposphere above and is the main subject of this study. All forcings on the heat and moisture budgets in the morning transition period are non-negligible, and therefore all must be considered when performing budget closure analysis (Angevine 2020).

Entrainment at the top of the boundary layer is particularly important in the morning transition. It occurs when rising convective thermals overshoot the boundary layer top, turbulently erode the capping inversion, and mix warm, dry free-tropospheric air downward, deepening the PBL and contributing strongly to its heat and moisture budgets (Stull 1998). Specific to the morning transition, entrainment also occurs due to PBL encroachment. As the PBL transforms into the daytime CBL, it deepens and grows upwards, engulfing air and residual layers aloft. The vertical motion also works to change the concentration of the air properties as the PBL deepens. This encroachment term is separate from the normal daytime turbulent mixing and can have a substantial impact on the heat and moisture evolution in the morning transition (Angevine et al. 2001; Blay-Carreras et al. 2014; Henkes et al. 2021, Rosenberger et al. 2025). These entrainment dynamics are depicted in detail in Fig. 1.3. In the morning, most of the warming in the mixed layer is due to mixing from above, whether from the upper part of the boundary layer or from entrainment (Angevine 2020). Observations from the Cabauw tower and subsequent analyses (Driedonks 1982; Angevine et al. 2001) showed that surface heat flux alone cannot explain the rapid erosion of the stable layer during the morning transition. Therefore, entrainment at the top of the boundary layer must provide the dominant source of warming. This is supported by other studies using modeling and indirect observations to diagnostically infer entrainment. Henkes et al. (2021) showed that while surface fluxes contribute during the morning transition, moisture entrainment may ultimately provide the dominant control on the development of the daytime convective boundary layer. Large-eddy simulations by Conzemius and Fedorovich (2006) further demonstrate the central role of heat and moisture entrainment in governing PBL growth, highlighting how entrainment is tightly coupled to surface fluxes.

A popular way to visualize heat and moisture budgets is to use mixing diagrams (MD). Betts (1984) first presented mixed layer heat and moisture budgets in two dimensional vector form, using conserved variable diagrams. These diagrams were particularly helpful for the depiction of the diurnal cycle of the dry mixed layer over land. This eventually led to the modern technique of mixing diagrams, which is one of the best methods used to understand heat and moisture budgets. Fig. 1.4 shows a modern example of a MD from Wakefield et al. (2023). MDs provide a way to describe CBL moisture and temperature budget evolution over any time period, and to quantify the relative contributions of surface fluxes, advection, radiative heating, and entrainment (Betts 1992; Santanello et al. 2009, 2011).

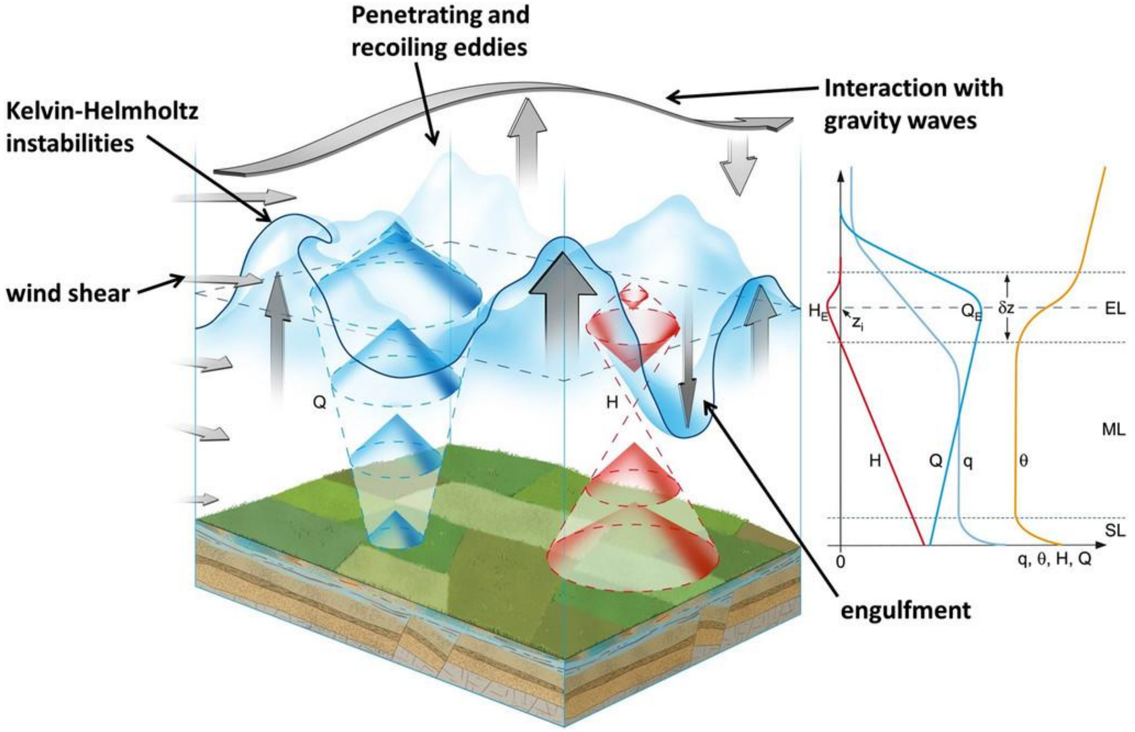

FIGURE 1.3: Schematic from Wulfmeyer et al. (2016) showing the many processes controlling how air from the free troposphere gets entrained into the boundary layer.

1.3 The Issue in Understanding Entrainment in the Morning Transition

Despite its importance, entrainment remains notoriously difficult to observe, particularly during the morning transition when the PBL is rapidly deepening and in situ sampling of the entrainment zone is challenging (Angevine et al. 1998). The entrainment zone is characterized by sharp gradients, small-scale variability, and motions occurring on much smaller spatial and temporal scales than interior boundary-layer turbulence, requiring exceptionally high-resolution measurements (Nelson et al. 1989; Cooper and Eichinger

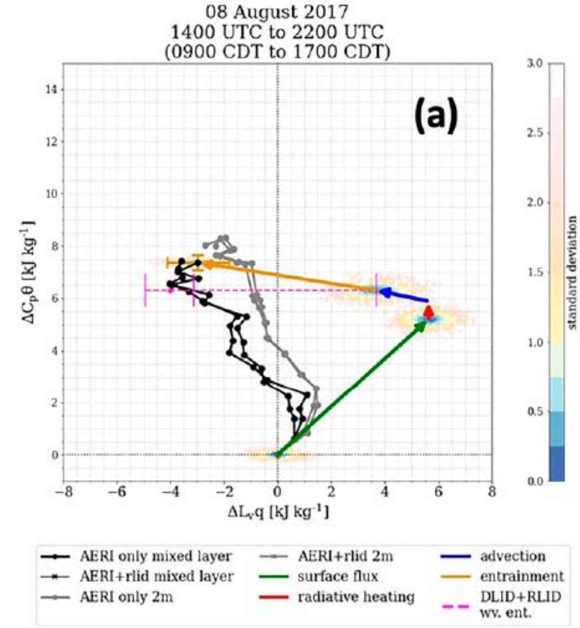

Figure 1.4: Example of a remotely-sensed mixing diagram of the daytime CBL from Wakefield et al. (2023).

1994; Liu et al. 2021). As a result, rates of entrainment cannot be measured directly and must be instead inferred from indirect observations, typically through budget methods (Lenschow et al. 1999), which previously have depended on uncertain estimates of advection often taken from models rather than observations (Angevine 1999; Santanello et al. 2005). The elevated position of the entrainment zone at the top of the boundary layer limits the ability to measure entrainment with ground-based remote sensing (Vilà-Guerau de Arellano, 2004), and insufficient instrument spacing and heterogeneous terrain cause difficulties in calculating horizontal averages (Driedonks 1982). Consequently, the fundamental physical mechanisms governing entrainment and their relationship to boundary layer properties remains poorly understood, and its representation in large-scale models causes a bias issue of the PBL being too cool and shallow due to insufficient entrainment

(Ayotte et al. 1996; Otte and Wyngaard 2001; Fedorovich et al. 2004, Angevine et al. 2020). To date, no large observational dataset of entrainment forcing in the PBL morning transition exists, preventing a systematic assessment of how entrainment varies across synoptic and environmental conditions.

Early efforts to observe entrainment relied on intensive field campaigns spanning only a few days, conducted before modern lidar systems were widely available. These studies typically used a series of radiosonde launches (Betts and Barr 1996; Barr and Betts 1998) or aircraft measurements (Betts et al. 1992; Grossman 1992) to infer entrainment parameters through budget methods and mixing diagrams. An influential parameterization study by André et al. (1978) found entrainment heat fluxes to be approximately 10–30% of surface fluxes under typical daytime convective conditions. Similar conclusions emerged from the Wangara experiment in Hay, Australia, where Yamada and Berman (1979) demonstrated that mixed-layer growth and heat budgets were well reproduced when entrainment heat flux was prescribed as 20% of the surface flux. Observations from Cabauw in the Netherlands further supported this value, as Driedonks (1981) showed that a 0.2 entrainment-to-surface flux ratio yielded the most accurate predictions of mixed layer height during the fully convective daytime periods. However, results from the First ISLSCP Field Experiment (FIFE) campaign over the Kansas prairie suggested substantially larger ratios. Using aircraft data, Betts et al. (1992) found values near 0.38 (±0.16) across additional cases, including some low-wind regimes—challenging the commonly assumed 0.2 ratio. The Flatland Boundary Layer Experiments similarly showed entrainment fluxes to be strong relative to surface fluxes and highly sensitive to synoptic influences such as wind shear and subsidence, although their mean results remained broadly consistent with the 20% parameterization (Angevine et al. 1998). More recently, the Land-Atmosphere Feedback Experiment (LAFE) conducted at the Atmospheric Radiation Measurement (ARM) Southern Great Plains (SGP) site in 2017 leveraged synergistic ground-based remote sensing systems to produce unprecedented 2D and 3D measurements of wind, temperature, and water vapor throughout the lower troposphere. This campaign enabled new insights into boundary layer dynamics and land-atmosphere feedback (Wulfmeyer et al. 2018). Much of the science produced by LAFE provides direct motivation for this study.

Despite the advances in understanding PBL entrainment from these studies and field campaigns, there is still doubt as to how true the entrainment to surface flux relationship is. The widely adopted Yonsei University (YSU) PBL scheme prescribes entrainment as 15% of the surface buoyancy flux (Hong et al. 2006; Wulfmeyer et al. 2016). The classical theory from field campaigns discussed above suggests the buoyancy flux ratio under idealized daytime conditions to be approximately 0.2. However, in more realistic boundary layer conditions the presence of gravity waves, wind shear, and subsidence are expected to exert strong controls on entrainment, calling into question the universality of a constant ratio (Wulfmeyer 1999a; Conzemius and Fedorovich 2006). Furthermore, because entrainment fluxes are difficult to measure, only a few observational studies are available to test model formulations, and those measurements that are available strongly suggest that entrainment flux as a fraction of the surface flux is quite variable (Angevine 2008).

Entrainment remains a major source of bias in boundary-layer modeling, particularly during the morning transition. Insufficient entrainment has been shown to produce PBLs that are systematically too cool and too shallow in models (Angevine et al. 2020). Baur et al. (2023) compared nested Weather Research and Forecasting model (WRF) simulations and lidar observations at the Department of Energy ARM SGP site, which revealed weaker-than-observed drying above the PBL and underestimated mixing into the boundary layer, mainly attributable to coarse vertical resolution in the model that fails to capture key entrainment-zone processes. Synoptic scale conditions may further complicate the bias issue of entrainment. A study by Banks et al. evaluated the sensitivity of model bias in WRF to various PBL schemes across different synoptic flow regimes. They found the model bias to differ substantially based on synoptic flow regime, shown in Fig. 1.5, with entrainment being a major limitation and source of uncertainty in the model. The bias difference between synoptic flow regimes was prevalent in the morning transition, suggesting that synoptic variability of entrainment in the morning transition may be a leading cause of the different model bias trends.

Furthermore, our limited understanding of entrainment fails to capture the finer nuances and differences of how it works in the morning transition. Much of our understanding of entrainment originates from field campaigns focused on the fully developed daytime convective boundary layer; however entrainment during the morning transition may exert a

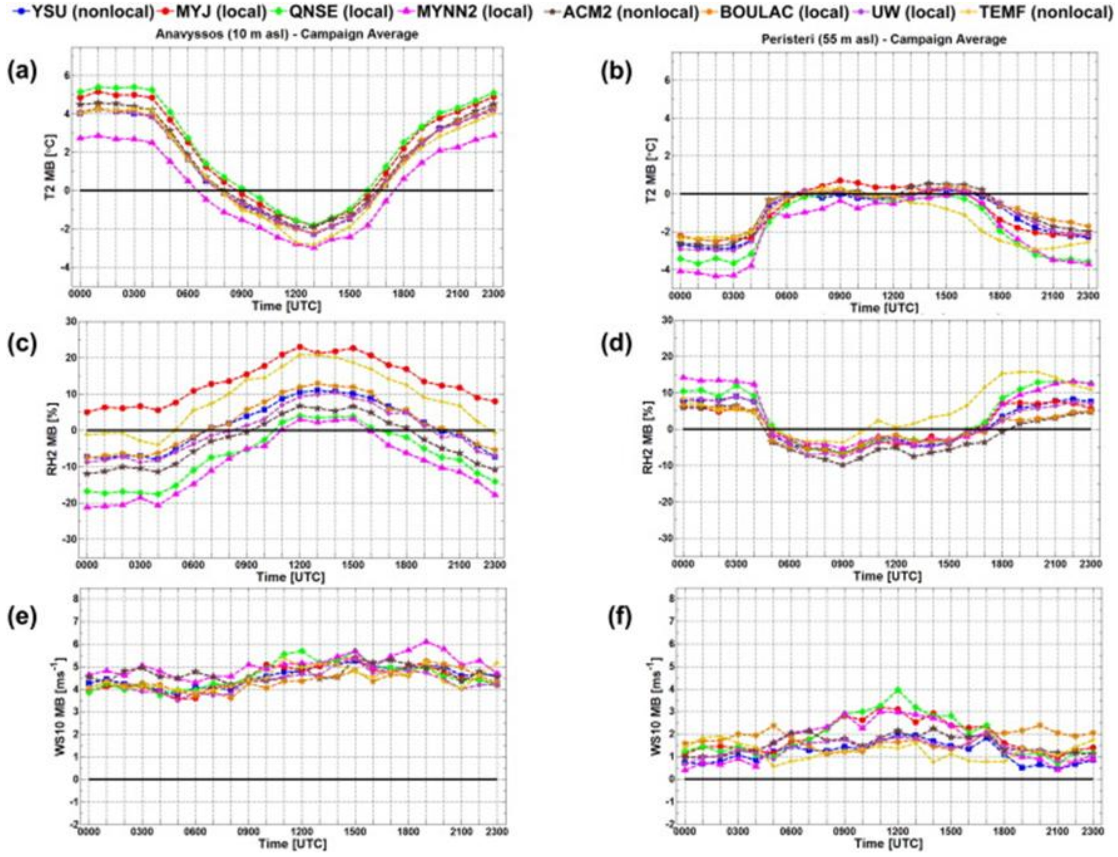

Figure 1.5: Plots from Banks et al. (2016) showing campaign-averaged WRF model mean bias for 2-m temperature, 2-m RH, and 10-m wind speeds at two different stations (Anavyssos and Peristeri), representing coastal and inland influences, respectively.

different influence on PBL evolution. Under idealized conditions, the ratio of entrainment to surface flux is expected to be substantially larger during the morning transition than during the daytime CBL (Angevine et al. 2001). Moreover, entrainment in mixed-layer budgets is typically treated solely as the turbulent flux across the PBL top. However, entrainment also includes the additional encroachment term as the mixed layer deepens, which becomes especially important during the morning transition and is necessary for closing mixed-layer budgets (Rosenberger et al. 2025). This suggests that total entrainment forcing in the morning transition differs markedly from its daytime counterpart and

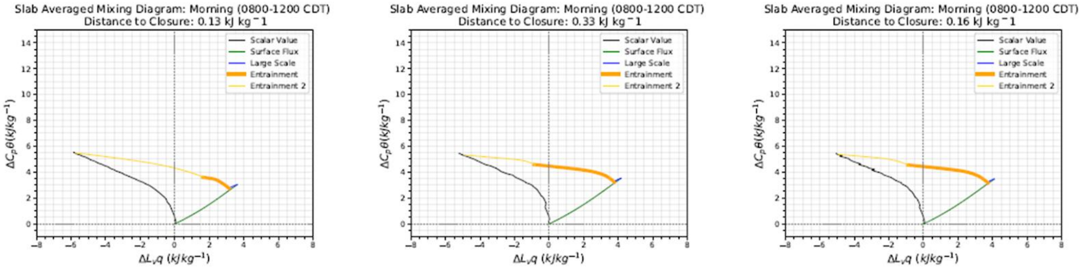

Figure 1.6: Mixing diagrams created from slab-averaged LES model output from Rosenberger et al. (2024). The thin orange component of the entrainment vector represents the encroachment term. This study shows encroachment as a substantial part of entrainment in the morning over three different PBL height definitions.

likely interacts with environmental conditions in distinct ways.

Morning boundary-layer growth is also influenced by the residual layer (Deardorff 1974; Sorbjan 1996; Blay-Carreras et al. 2014), and its impact on entrainment is not fully captured in entrainment theory focused on daytime conditions. Using FIFE observations, Freire et al. (2013) demonstrated that the residual layer substantially alters mixed-layer growth in slab models, decoupling entrainment behavior from surface fluxes. Large-eddy simulations and observations from the Boundary-Layer Late Afternoon and Sunset Turbulence campaign (BLLAST) further show sudden boundary-layer deepening when the mixed layer grows into a well-defined residual layer, emphasizing the importance of nocturnal boundary-layer dynamics for subsequent morning evolution (Blay-Carreras et al. 2014). Residual-layer entrainment has also been identified as a key control on the potential for deep convection later in the day (Henkes et al. 2021).

In summary, while entrainment is clearly central to morning-transition boundary-layer development, uncertainties remain regarding how it varies with local and synoptic-scale conditions. This knowledge gap continues to limit effective parameterization in numerical models, contributing to biases and motivating the need for observation-based characterization of entrainment forcing during this critical transition period.

1.4 New Opportunities Through Advancements in PBL Measurements

Recent advances in ground-based remote sensing have expanded our ability to observe planetary boundary layer (PBL) structure with high temporal and vertical resolution. Early work by Wilczak et al. (1996) emphasized that much of the progress in understanding PBL transitions has been driven by ground-based remote sensing observations. Building on this foundation, an innovative network of scanning remote sensing instruments was introduced at SGP that is capable of providing comprehensive, model-independent datasets to characterize land-atmosphere feedback (Wulfmeyer et al. 2018). These observational capabilities now allow detailed characterization of thermodynamic evolution, turbulence, and boundary layer growth across diurnal transitions at the SGP site in north central Oklahoma. This site experiences diverse synoptic-scale weather patterns, due to the El Nino Southern Oscillation (ENSO) climate variability pattern having an outsized influence on weather patterns over the Southern Great Plains (Ropelewski and Halpert 1986), as well as synoptic scale influences from the Great Plains Low Level Jet (LLJ). However the site also has a homogeneous landscape characterized by grazing fields and wheat crops, posing it as an excellent site to study local land-atmosphere interactions and how synoptic conditions can influence them.

Despite these advances at SGP, closing the heat and moisture budgets of the PBL has historically remained challenging. Numerous studies (Kustas and Brutsaert 1987; Peters-Lidard and Davis 2000; Santanello et al. 2005) have shown that, aside from entrainment, horizontal advection represents a dominant source of uncertainty in PBL energy budgets. Until recently, advection was often estimated or ignored in observational frameworks such as mixing diagrams. However, recent developments by Wagner et al. (2022) now allow observational estimates of advection, enabling closure of heat and moisture budgets through observations with entrainment as the only unknown. This breakthrough allows entrainment forcing to be diagnosed directly as the residual of the budget, representing the combined effects of turbulent mixing and PBL encroachment.

These advances have developed the mixing diagram framework as a diagnostic tool. Wakefield (2023) demonstrated the feasibility of constructing mixing diagrams using the comprehensive suite of remote sensing instruments at the ARM SGP site, establishing a pathway for retrieving entrainment forcing from observations. With accurate advection measurements available, this approach can be extended beyond the daytime convective boundary layer to the morning transition period. For the first time, this enables observation-based estimates of total entrainment forcing during the morning transition over SGP, opening new opportunities to investigate the physical controls on this critical phase of boundary layer diurnal evolution.

1.5 Research Objectives

There has been much focus on understanding entrainment as a ratio to surface buoyancy flux; however, the resulting relationship may only hold true for the daytime CBL, and there is much doubt in the literature as to how true the relationship is. Entrainment is influenced by a broader set of factors, including large-scale atmospheric conditions and environmental variability, such as soil moisture, wind shear, gravity waves, and subsidence, which are not yet well understood. Moreover, entrainment during the morning transition may behave much differently than during the daytime CBL, owing to residual layer interaction and PBL encroachment. Despite its importance, morning transition entrainment has received relatively little attention, largely due to observational limitations. The development of a large observational dataset of morning transition entrainment forcings at SGP therefore represents an opportunity to explore these uncertainties. The primary research questions addressed in this study are:

1. How does the entrainment forcing in the PBL morning transition vary with land and synoptic-scale atmospheric conditions?

2. How do processes unique to the morning transition impact the entrainment forcing?

To address these questions, this study applies the mixing diagram technique with entrainment diagnosed as the residual of the heat and moisture budgets, producing a dataset of morning transition entrainment forcings. This dataset is analyzed alongside key environmental variables from remote sensing, radiosonde observations, and reanalysis data products. In addition, targeted case studies are used to show nuances of the PBL structure and to explore the physical mechanisms governing entrainment during the morning transition. The results will help determine whether entrainment during the morning transition exhibits variability consistent with existing parameterizations or whether distinct relationships emerge, thereby informing future model development and improving representation of diurnal boundary layer processes.

Chapter 2

Data and Methods

This chapter starts by describing the observational datasets used in this study and then explains the details of the mixing diagram (MD) and self-organizing map (SOM) methods.

2.1 Observational Site: DOE ARM Southern Great Plains

All the observational data are obtained from instruments at the Department of Energy Atmospheric Radiation Measurement (ARM) site in the Southern Great Plains (SGP), located in central Oklahoma near the town of Lamont. The SGP site has a flat, heterogeneous landscape consisting mainly of cattle pasture and wheat crops. ARM SGP is equipped with a vast wealth of remote sensing instruments, facilitating advanced observations of the boundary layer and lower troposphere for many different applications.

2.2 AERI

Data from the Atmospheric Emitted Radiance Interferometer (AERI) instrument are a fundamental part of the observations for this study. AERI is a ground-based remote sensing instrument that measures downwelling spectral infrared radiation with a spectral resolution of 0.5 cm-1 and a maximum sample frequency of approximately twice per minute (Knuteson et al. 2004). The Tropospheric Remotely Observed Profiling via Optimal Estimation (TROPoe) is used to retrieve thermodynamic profiles from the AERI spectral radiance observations (Turner and Löhnert 2014; Turner and Blumberg 2019). An advantage of this optimal estimation framework is that it provides quantified uncertainties and error characterization for each retrieved variable. Typical uncertainties from TROPoe retrievals in the lower half of the mixed layer are 0.4 K and 0.8 g/kg for temperature and moisture, respectively (Blumberg et al. 2017). These uncertainties can be used in the calculation of derived variables, as well as land-atmosphere coupling metrics (Wakefield et al. 2021). In this study, the uncertainty derived from TROPoe is useful for propagating into the uncertainty of the entrainment residual from the mixing diagram approach described below. This study uses AERI retrieved thermodynamic profiles collocated at the central facility of ARM SGP during 2018 and 2019.

2.3 Doppler Lidar

The Doppler lidar (DL) is an instrument used in this study to observe the vertical profile of wind, which can be used to calculate horizontal advection rates of potential temperature and water vapor mixing ratio. The DL is an active remote-sensing instrument that measures range and time-resolved radial velocity and attenuated aerosol backscatter by transmitting short pulses of near-infrared laser light into the atmosphere. Aerosols scatter a portion of this light back to the instrument, and the time delay between transmission and return is used to determine distance. Radial velocity is derived using coherent detection, in which the backscattered signal is mixed with a reference beam to measure the Doppler frequency shift from the signal spectrum. From this, observations at a fixed elevation angle at different azimuths can be used to determine the vertical wind profile. The DL provides reliable measurements in regions with sufficient aerosol loading—typically within the atmospheric boundary layer. With full scanning capability, the instrument can map three-dimensional wind fields, while vertical stares provide high-resolution profiles of vertical velocity (Newsom et al. 2022).

2.4 Surface Flux Observations: ECOR

This study uses the Eddy Covariance (ECOR) flux measurement system to measure sensible and latent heat fluxes in 30 minute intervals. Turbulent fluxes are derived from the 30-minute averaged covariances of vertical velocity and scalar thermodynamic variables (Cook and Sullivan 2020). The ECOR system is located at the central facility at ARM SGP, collocated with the AERI and radiosondes used in this study. Calibration uncertainties of 5% for sensible heat flux and 6% for latent heat flux exist in the ECOR measurements (Cook and Sullivan 2020), which will be propagated into the uncertainty of the entrainment residual in the mixing diagram framework . A quality-controlled value added product (QCECOR) was introduced to correct known shortfalls of 10%-25% in observed fluxes (Tang et al. 2019; Cook and Sullivan 2020), resulting in improvements to PBL budget closure. Surface fluxes from the corrected QCECOR dataset are used in this study.

The mixing diagram method from Wakefield et al. (2024) calculates surface fluxes as the average of both ECOR and the Energy Balance Bowen Ratio (EBBR) system collocated at ARM SGP. The mixing diagram method in this study follows closely to that in Wakefield et al. (2024); however a key difference in this study is that the surface fluxes are calculated using only the ECOR system. The EBBR system calculates surface fluxes by solving the surface energy balance and partitions the available energy using the Bowen ratio. However, in the early morning evolution, sensible heat flux changes sign and latent heat flux ramps up quickly, causing a very large or undefined Bowen ratio, resulting in unrealistic spikes in calculated surface fluxes (Tang et al. 2019). Furthermore, many EBBR datasets flag or remove data from the morning period for this reason. Wakefield et al. (2024) applied the mixing diagram method only to the daytime CBL state, intentionally not capturing the morning or evening transitions. Because this study is applying the mixing diagram method directly to the morning transition, the EBBR system can not be used to obtain accurate surface flux measurements, and therefore the ECOR system is the sole source of surface flux data used in this study.

2.5 Advection Observations: AERI + Doppler Lidar

Advection is an important component of mixing diagram (MD) analyses, but it has historically been difficult to quantify, especially when advection in a vertical structure is needed for a mixed-layer mean analysis like the one used in this study. However, recent work by Wagner et al. (2022) addressed this limitation by using a finite approximation to Green's theorem to calculate advection from AERI retrievals combined with collocated Doppler lidar measurements at the ARM SGP site.

$$\oint_C P\,dx + Q\,dy \;=\; \iint \left(\frac{\partial Q}{\partial x} - \frac{\partial P}{\partial y} \right) dA \tag{2.1}$$

Green's theorem is shown in Eqn. 2.1, where a line integral of a boundary is related to the integral of the area inside. Using this equation, the line integral on the LHS, computed at SGP with the collocated instruments, can approximate the RHS of the equation. Using the correct substitution of the placeholders P and Q for this method, the line integral can be used to approximate kinematic profiles of vorticity, deformation, divergence, and heat and moisture advection. The Doppler lidar horizontal wind profiles are retrieved via an optimal estimation technique (Baidar et al. 2023), providing coverage throughout the full depth of the boundary layer. These wind profiles are interpolated onto the vertical grid of the TROPoe retrievals, and advection is calculated independently at each level to obtain profiles of temperature and moisture advection. Uncertainty in both thermodynamic and kinematic fields is quantified through Monte Carlo sampling. This framework yields advection estimates at vertical levels within the PBL, enabling improved representation of advection in moisture and energy budgets across the mixed layer. The resulting advection data product for years 2018 and 2019 are used to compute the advection component of the budgets in this study. The approach used to measure advection in Wagner et al. 2022 requires 6 different instruments to operate simultaneously. This requirement leads to issues in data availability due to the difficulty of observing cases with the entire synergy of sensors operating properly. This results in missing cases within the available 2018 and 2019 dataset; in particular there are no cases in November through December in both years.

2.6 Mixed Layer Definition

The mixed layer definition in this study follows the same definitions in Wakefield et al. 2023. The main innovation by Wakefield is that the entire mixed layer of the PBL is considered instead of only 2 m observations. The defined mixed layer in this study is the area over which the vertically averaged evolution of heat and moisture is observed in the heat and moisture budgets. It is defined as the area between 0.1zi and 0.5zi, where zi denotes the height of the PBL. The lower limit of 0.1zi is defined to avoid sampling of the surface layer, which is typically within the lowest 10% of the PBL. The upper limit of 0.5zi is chosen to avoid sampling of the entrainment zone, and minimizes the bias from the AERI-derived temperature and moisture profiles, as the bias has been shown to increase rapidly above the limit of 0.5zi (Blumberg et al. 2017).

2.7 Mixing Diagrams

The mixing diagram framework in this study follows the same conservation formula derived for the mixed-layer heat and moisture budgets of Eq. 4 in Wakefield et al. (2023):

$$k\frac{\partial\langle\bar{\phi}\rangle}{\partial t} = k\left\langle -\mathbf{v}\cdot\nabla_h\phi\right\rangle + \frac{gF_s}{d_p} + \frac{gF_i}{d_p} + \frac{gk\overline{\rho W_e(\phi_i - \langle\bar{\phi}\rangle)}}{d_p} + k\left\langle Q_R\right\rangle \tag{2.2}$$

Where ϕ is the scalar of potential temperature or water vapor mixing ratio, k is the scaling constant (C_p or L_v), $\partial\langle\bar{\phi}\rangle/\partial t$ is the time tendency of the scalar, $\langle -\mathbf{v}\cdot\nabla_h\phi\rangle$ is the horizontal advection of the scalar, F_s is the surface sensible and latent heat flux, and $k\langle Q_R\rangle$ is the radiative heating component of the heat budget. The two terms

$$\frac{gF_i}{d_p} + \frac{gk\overline{\rho W_e(\phi_i - \langle\bar{\phi}\rangle)}}{d_p}$$

represent the turbulent mixing and encroachment terms of entrainment, respectively, and are considered collectively as the total entrainment in the mixing diagram analysis. This equation provides the overall framework of how each vector of the mixing diagram is partitioned to equate to the total time tendency of the scalar over the mixed layer. The result in graphical format is shown in Fig. 2.1, which shows a representative mixing diagram constructed for the morning transition for a particular case.

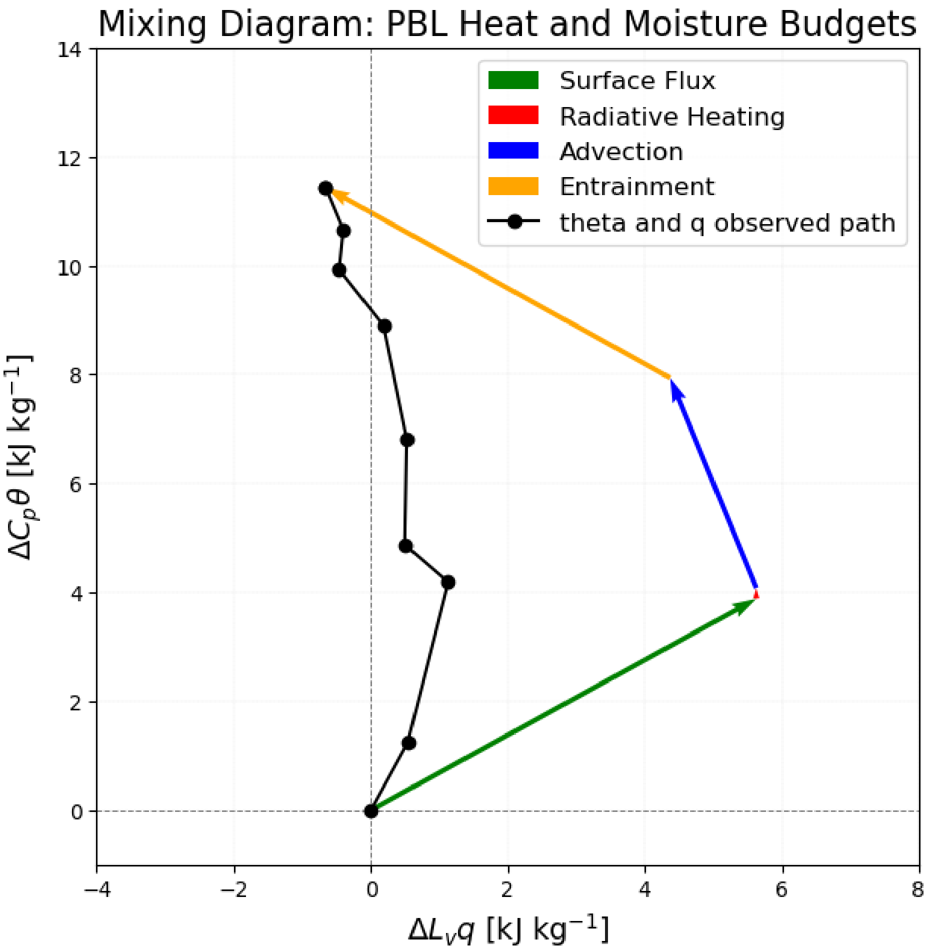

FIGURE 2.1: Representative case of a mixing diagram constructed from remote sensing observations at SGP. This case was on 22 March 2019, and the mixing diagram represents the morning evolution from 1230 to 1630 UTC.

2.7.1 Graphical Representation: Moisture and Temperature Evolution

The evolution of potential temperature and moisture in the mixed layer is represented by the black curve in the mixing diagram. Each point on the curve represents the average heat and moisture content within the mixed layer at that time, and the points are in

30 minute intervals. The values come from thermodynamic profiles derived from AERI, with the y-axis representing the mean mixed layer potential temperature multiplied by the specific heat capacity, and the x-axis representing the mean mixed layer water vapor mixing ratio multiplied by the latent heat of vaporization. Each point is subtracted by the starting values of heat and moisture to standardize the curve to start at zero for each.

2.7.2 Graphical Representation: Surface Fluxes

The surface flux vector reflects the contribution of both latent and sensible heat fluxes toward the PBL evolution. They are calculated as the mean surface fluxes during the analysis period scaled by the mean boundary layer depth. The x component of the vector is computed by multiplying the mean surface latent heat flux by the length of the time period in seconds and dividing by the mean boundary layer depth over the time period. The y component is calculated in the same way, but by replacing the mean latent heat flux with the mean sensible heat flux.

2.7.3 Graphical Representation: Advection

The advection vector represents the overall contribution of the heat and moisture evolution of the mixed layer by horizontal advection. Advection data comes from the advection product created from Wagner et al. (2022), which is discussed above in greater detail. The advection data is in rates on multiple vertical levels within the PBL at 30 minute intervals. The advection vector is calculated by taking the average advection rate over the mixed layer at each time step and multiplying it by the length of the time step, then summing them all over the total observation period.

2.7.4 Graphical Representation: Radiative Heating

Radiative heating is represented in the heat budget as the small red dot in the mixing diagram in Fig. 2.1. The radiative heating component of the heat budget can be computed directly using TROPoe-retrieved thermodynamic profiles in a short and longwave version of the RRTM radiative transfer model (Mlawer et al. 1997; Iacono et al. 2008) to compute profiles of total radiative heating rate within the PBL. To be consistent with Wakefield et al. (2023) an aerosol optical depth (AOD) of 0.4 was assumed for all cases in the RRTM model. The radiative heating vector is then obtained by summing the product of the mixed-layer mean radiative heating rate and time step for all time steps in the period. This total radiative heating amount is then multiplied by the specific heat capacity to get the energy impact on the heat budget. The total radiative heating contribution to the heat budget is small, especially in the morning transition when the sun angle is low and the PBL is shallow. For example, the case occurring on 12 June 2019 had a radiative heating contribution of 0.06 kJ/kg in the morning hours between 12:30 and 16:30 UTC, whereas the radiative heating contribution during the daytime hours of 16:30 to 20:30 UTC on this day was 0.23 kJ/kg. Although the radiative heating is small in the morning transition, it is still an important component to consider in the heat budget.

2.7.5 Graphical Representation: Entrainment

The entrainment vector in the mixing diagram is calculated as the residual amount between the evolution of the mixed layer heat and moisture and the sum of the other vector components. This vector represents the total energy contribution to the heat and moisture budgets from total entrainment, including both the turbulent mixing and encroachment terms in Eqn. 1. During typical clear air entrainment, we expect to see positive energy contributions for the heat budget and negative contributions for the moisture budget, because entrained air from the free troposphere is typically warmer and drier than the mixed layer.

2.8 Uncertainty Calculation

The uncertainty in entrainment quantification using this mixing diagram framework is an important consideration. The uncertainty structure is difficult to quantify analytically because the entrainment estimate depends on several instruments with distinct error characteristics that interact non-linearly within the mixing diagram framework. Therefore, a Monte Carlo approach is well-suited, as it enables repeated random sampling from each measurement's uncertainty distribution and captures how these combined uncertainties propagate into the final entrainment estimate. To calculate the uncertainty, a Monte Carlo approach is used that propagates the uncertainties of all the distributions of the measurements with a standard deviation of the uncertainty of that measurement. Each randomly sampled simulation constructs a mixing diagram, and consequently an entrainment estimate through the budget closure. This randomly sampled mixing diagram is repeated for 1000 simulations, resulting in 1000 randomly sampled entrainment estimates. A sample size of 1000 simulations provides a stable estimate of the resulting uncertainty distribution, as the Monte Carlo mean and standard deviation converge sufficiently while keeping computational costs reasonable. The standard deviation of this set of randomly sampled entrainment estimates is taken to be the uncertainty for the case. The same mixing diagram case shown in Fig. 2.1 is shown in Fig. 2.2 with error bars included for each vector showing the resulting uncertainties from applying this Monte Carlo approach.

The TROPoe retrievals for thermodynamic profiles used in calculating the heat and moisture evolution of the mixed layer include uncertainties for both scalars. These uncertainties are propagated into the monte carlo sampling for the starting and ending value of mean mixed layer potential temperature and water vapor mixing ratio for the period of study. For surface fluxes, latent heating measurements from ECOR have an uncertainty of 6%, and sensible heat has an uncertainty of 5% (Cook and Sullivan 2020). The PBL height is also a parameter in the calculation of surface fluxes, as the total energy contribution from them is standardized by PBL height. Therefore, the uncertainty in PBL height propagates through random sampling of the surface fluxes. The advection data product contains uncertainties in the derived water vapor and potential temperature advection rates which are calculated themselves with a Monte Carlo approach (Wagner et al. 2022). However, the advection data also contains a posterior covariance matrix with

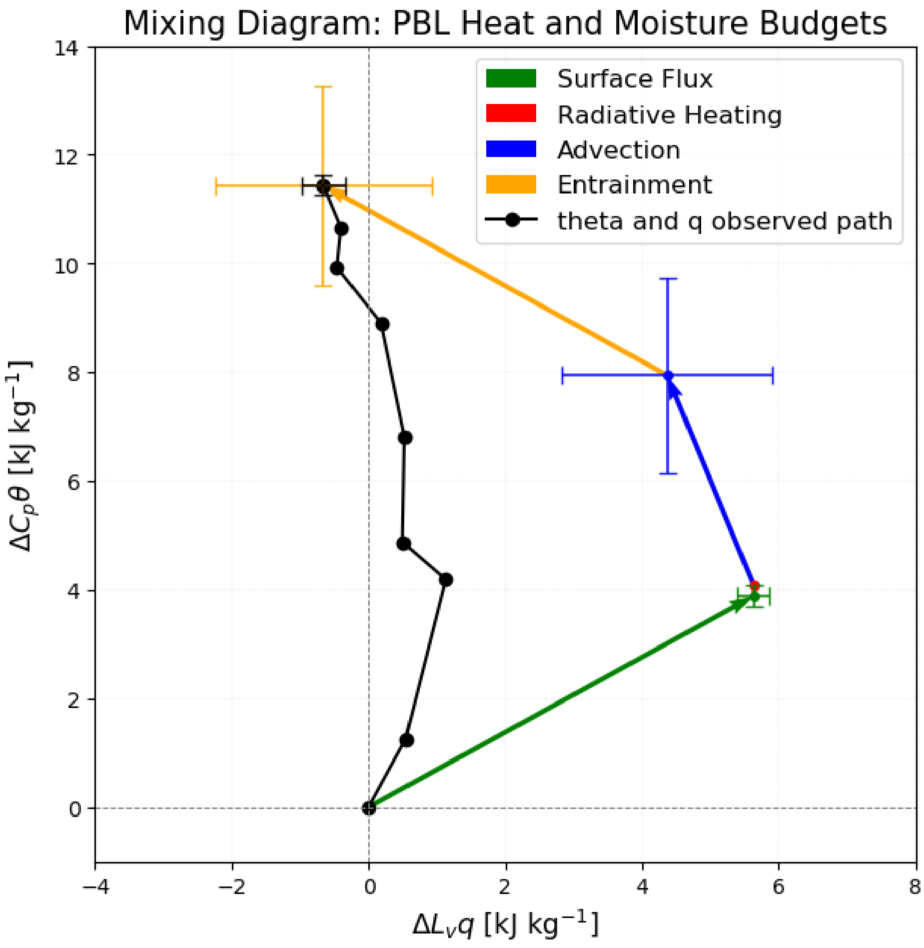

FIGURE 2.2: The same mixing diagram from Fig. 2.1 with errors bars resulting from applying the Monte Carlo method for calculating uncertainties in the budget terms and resulting entrainment estimate.

the TROPoe thermodynamic retrievals that is also randomly sampled and propagated through to the total uncertainty in the advection budget term.

2.9 Case Definition

Due to the complicated nature of the mixing diagram method and the sensitivity of the instruments involved, having strict case selection criteria is critical for the method to be valid. Each case is defined as the time window of sunrise to four hours after sunrise specific to each day. There must be no precipitation, no active synoptic fronts, and a cloud fraction of less than 20% if the cloud base height is less than 4km to avoid low level cloud entrainment processes. Furthermore, all instruments need to be functioning properly throughout the entire time period with reasonable accuracy. A threshold of 2 kJ/kg of uncertainty is enforced for the final entrainment estimate, with any cases of entrainment with uncertainty greater than that being removed.

2.10 Self-Organizing Maps (SOMs)

This study uses Self-Organizing Maps (SOM) to categorize cases by synoptic-scale conditions. The large-scale meteorological data used to construct the SOMS came from the European Centre for Medium-Range Weather Forecasts (ECMWF) ERA5 reanalysis dataset (Hersbach et al. 2020). ERA5 provides hourly, gridded atmospheric fields with global coverage and high spatial resolution. For this study, a regional subset centered on the ARM SGP site was extracted. The variables from ERA5 used to define synoptic-scale conditions were mean sea level pressure (MSLP), 10-m zonal wind (u10), and 10-m meridional wind (v10). These fields were selected because they capture the near-surface pressure gradient and associated flow patterns that govern boundary layer forcing. To ensure consistency with the observational analysis, ERA5 data were filtered to include only days corresponding to the available entrainment cases.

Before the main SOM algorithm, preprocessing and feature construction were performed.

For each retained time step, the mean sea level pressure (MSLP) field was reshaped from a two-dimensional latitude–longitude grid into a one-dimensional feature vector, where each vector represents the spatial pressure pattern at that time step. To ensure equal weighting across spatial features, all MSLP values were normalized using min–max scaling:

$$x' = \frac{x - x_{\min}}{x_{\max} - x_{\min}} \tag{2.3}$$

This normalization prevents large absolute pressure values from dominating the clustering process and ensures that the SOM is sensitive to spatial patterns rather than magnitude alone. These normalized values were then used in the SOM algorithm, an unsupervised neural network that groups high-dimensional data onto low-dimensional discrete nodes while preserving the multi-dimensional features of the data.

The algorithm works by initializing random weights and training on the normalized MSLP vectors. The training procedure follows the standard SOM iterative process:

$$\mathbf{w}_i(t+1) = \mathbf{w}_i(t) + \alpha(t)\, h_{ci}(t)\ [\mathbf{x}(t) - \mathbf{w}_i(t)] \tag{2.4}$$

where $\mathbf{w}_i$ is the weight vector for node i, $\alpha(t)$ is the learning rate, $h_{ci}(t)$ is the neighborhood function centered on the best matching unit (BMU), and $\mathbf{x}(t)$ is the input vector at iteration t. The parameters chosen for the SOM algorithm used in this study include a learning rate of 0.5, neighborhood width of 1.0, and 1000 training iterations. These parameters were selected to produce a simple, interpretable classification of synoptic-scale regimes. After training, each ERA5 time step was assigned to a SOM node by identifying the best matching unit (BMU), defined as the node whose weight vector minimizes the distance to the input vector. Each day in the dataset was therefore classified into one of two synoptic regimes. Then, for each SOM node, composite fields of MSLP and 10-m winds were computed by averaging all ERA5 fields assigned to that node. These composites were used to visualize the characteristic synoptic structure associated with each regime, including pressure patterns and near-surface wind fields. Additionally, monthly case counts were calculated by grouping days by calendar month and node membership to analyze seasonal variability of each SOM node.

Chapter 3

Results

3.1 Synoptic and Surface Dependence of Morning Entrainment

Using the mixing diagram method, a dataset of morning transition PBL entrainment forcings in energy units [kJ/kg] was constructed, consisting of 61 cases. The entrainment forcings represent the total energy input to the mixed layer value due to entrainment. Physically, clear air PBL entrainment is expected to consist of warm, dry air relative to the mixed layer in the morning transition (Davis et al. 1997). Warm air entrainment in the results is signified as a positive energy value in the heat budget, and dry air entrainment is signified as a negative energy value in the moisture budget. Table 3.1 displays the average values and standard deviations for each potential temperature and water vapor forcing in this study to show the relative magnitude for each. The resulting dataset will be used throughout this study to address the proposed questions on the synoptic and environmental variability of entrainment and the unique aspects of entrainment over the morning transition. To address the question of synoptic and large-scale influence on morning entrainment, we first need to categorize the cases into different synoptic regimes. This is accomplished by applying the self-organizing map (SOMs) technique to horizontal winds and mean sea level pressure from the ERA5 reanalysis for the 4 hour morning window for each case used in this study. The technical aspects of the SOM method are discussed in detail in the methods section 2.10. Building the SOMs results in a set number of nodes that group similar synoptic-scale conditions together; the mean state for each node is thus a representative value for each state in the node. The analysis in this study uses 2 SOM nodes in this study for synoptic categorization, which was motivated by multiple reasons. First, when examining the results with various amounts of synoptic nodes, distinct results were consistently observed in similar nodes of high-pressure and anticyclonic wind patterns, as well as low-pressure pattern nodes. Figure 3.1 displays the results of categorizing water vapor entrainment using 4 nodes, resulting in distinctly weaker entrainment within nodes 3 and 4, as well as distinctly stronger entrainment within nodes 1 and 2. Therefore, the two-node approach was chosen to

	Theta Entrainment	WV Entrainment	Theta Advection	WV Advection	Sensible Heat Flux	Latent Heat Flux	Radiative Heating
Mean Value	2.39	-3.61	-0.57	0.19	5.13	3.347	0.02
SD	2.17	2.61	2.04	0.96	2.03	2.22	0.20

Table 3.1: Mean value and standard deviation in kJ/kg over all 61 cases for each mixed layer heat and moisture budget term calculated in this study.

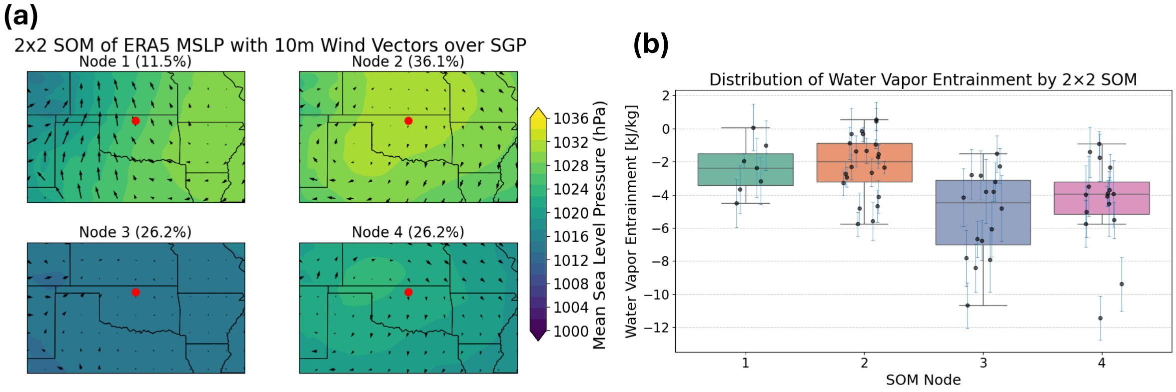

Figure 3.1: (a) The resulting pressure/wind maps of 4 SOM nodes and (b) forcings of water vapor entrainment categorized into the 4 SOM nodes.

isolate the observed effect of this pressure pattern, and provide the most intuitive analysis of the role of synoptic conditions on entrainment. Also, a lower SOM node count of 2 is more appropriate for the case count of 61 in this study. Using self-organizing maps, even with a lower node count, is important because it preserves the multi-dimensional nature of synoptic conditions defined in this study. Grouping cases by an average pressure threshold would ignore the finer nuance of synoptic patterns that exists within the cases. Using the two-node approach, the resulting SOM nodes from this method resemble one node with a lower pressure pattern, and one node with higher pressure and anticyclonic wind pattern. These SOM nodes and corresponding monthly distribution of cases are displayed in Fig. 3.2. The mean difference in sea level pressure between the two nodes is 10.83 hPa. These nodes categorize cases into the respective synoptic conditions; hereafter referred to as the high-pressure node and the low-pressure node, respectively. The high-pressure node contains 31 cases, and the low-pressure node contains 30 cases, resulting in the two SOM maps and the distribution of case counts per month for each node. The

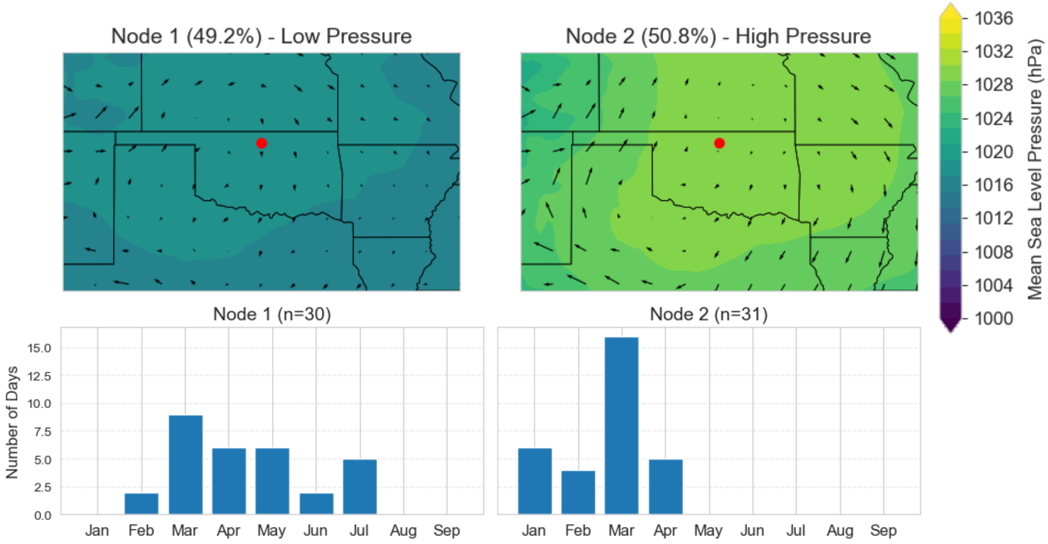

Figure 3.2: Self organizing map nodes for synoptic regime classification resulting from ERA5 surface winds and pressure data, with case counts by month for each node.

total cases available for this study span only the months of January to July. In the monthly spread, there is some observed seasonality to the nodes, with the high-pressure node containing more winter months and the low-pressure node containing more summer months. However, there is strong overlap in the seasonality of the nodes, noting February cases in node 1, and a substantial overlap with March and April days making up 15 cases in node 1 and 21 cases in node 2.

By categorizing the entrainment dataset into the two synoptic nodes, entrainment forcings can be analyzed in the context of synoptic conditions. Fig. 3.3 displays the spread in entrainment forcing between the synoptic nodes. The error bars are calculated by taking the standard deviation of the spread of entrainment estimates from 1000 Monte Carlo simulations for each case, leveraging the known uncertainties for each measurement. This calculation is described in detail in the methods section. The average uncertainty in

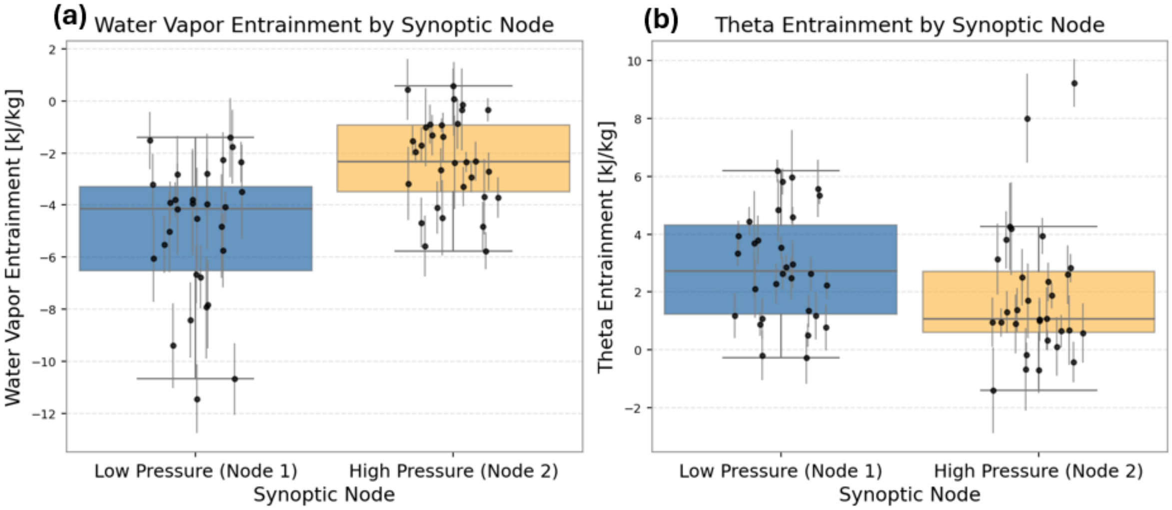

Figure 3.3: Results of entrainment forcing in the morning transition over all 61 cases grouped by synoptic node for (a) water vapor entrainment and (b) theta entrainment. Error bars included as the standard deviation from 1000 simulation Monte Carlo sampling.

entrainment value is 1.16 kJ/kg for water vapor and 0.82 kJ/kg for potential temperature. These values are similar to entrainment uncertainty found in Wakefield et al. (2023), which uses a similar mixing diagram method to the one used in this study. For both water vapor and potential temperature, weaker entrainment forcings are observed in the high-pressure node and larger, more variable forcings are observed in the low-pressure node. To test the statistical significance of whether entrainment differs between synoptic regimes, a two-sample Welch's t-test was performed comparing the entrainment forcings between the synoptic nodes. Welch's test was chosen to account for the unequal sample sizes between nodes. For water vapor entrainment, the difference in mean value between nodes was statistically significant (p ¡ 0.05), indicating a substantial impact from synoptic conditions. The difference in potential temperature entrainment approached significance (p = 0.056) at the 95% level, suggesting a weaker synoptic influence compared to water vapor.

Together, these results demonstrate that while both scalars exhibit some sensitivity to synoptic nodes, water vapor emerges as the dominant contributor to synoptic variability in mixed-layer energetic input by entrainment during the morning transition. The dominance of water vapor in synoptic variability of entrainment in the morning transition may be due to a combination of factors that will be explored in the subsequent sections. Since converting water vapor perturbations into energy units weights it by the latent heat of vaporization (Lv) factor, which is much greater than specific heat capacity, smaller variations in moisture produce stronger energetic impacts to the mixed layer than potential temperature. This may be amplified by vertical moisture gradients that are typically sharper than potential temperature vertical gradients in the morning from nighttime decoupling of the residual layer. Furthermore, the encroachment term of entrainment in the morning transition creates a sensitivity to changes in column temperature and moisture above the PBL, of which moisture can be modulated stronger from advection. Together, these factors can make water vapor entrainment highly sensitive to synoptic conditions, explaining its amplified variability.

To investigate this hypothesized role of vertical gradients driving entrainment variability with remote sensing observations, AERI-derived vertical profiles of water vapor and temperature, standardized to the mixed layer mean for each, are analyzed. The standardized gradients represent how quickly the properties of the air change above the mixed layer

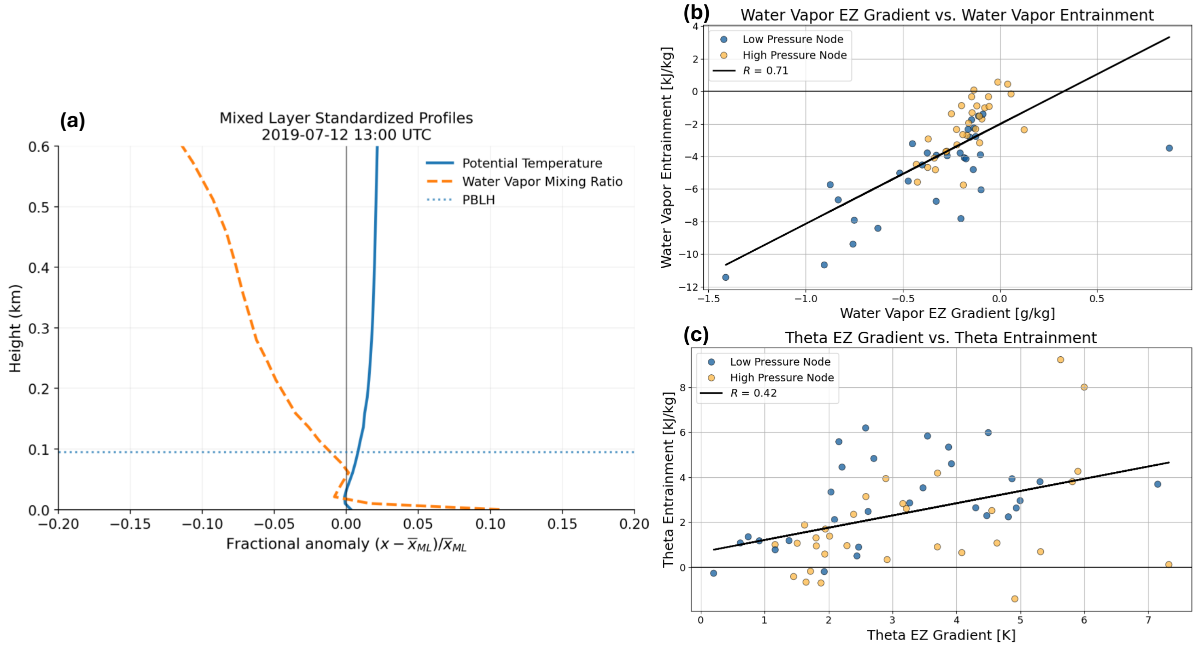

FIGURE 3.4: (a) A case showing a good representation of the vertical profile of theta and water vapor mixing ratio anomalies, standardized to the mixed layer mean for each variable. (b) Water vapor entrainment values regressed on the water vapor gradient from 50m below to 100 m above the PBL height at sunrise (c) similar regression, but with theta entrainment regressed on the theta gradient. Both color coded by synoptic node.

with height. Using this method, it is observed in Fig. 3.4a that the standardized negative gradient of water vapor mixing ratio around the PBL height is much sharper than the positive gradient in potential temperature during the morning transition. Fig. 3.4a shows a representative case of this difference in gradient. To quantify the water vapor and potential temperature gradients across the entrainment zone (EZ), a measure of the gradient value from 50 meters below to 100 meters above the estimated PBL height is taken. Taking the gradient in this zone will sufficiently capture the magnitude of the gradient in water vapor and potential temperature across the EZ, which is known to have a thickness on the order of tens to a few hundred meters (Davis et al. 1997; Pal et al.

2010). Larger gradient zone measurements were tested in this study as well, where similar but weaker results were produced. The entrainment values of water vapor and potential temperature for each case are regressed against their respective gradient variables, shown in Fig. 3.4b and 3.4c. The results in these figures show the entrainment rates of water vapor follow strongly to its respective gradient at sunrise, with an r value of 0.71. However, potential temperature entrainment values do not have as highly correlated of a relationship to the potential temperature gradient values at sunrise with an r value of 0.42. These results show that water vapor entrainment appears to be more sensitive to vertical gradients than potential temperature entrainment. Of note is an outlier in the water vapor gradient included in the cases, observed as the farthest right dot in the water vapor regression chart in Fig. 3.4b. The nuances of this case will be the subject of a later case study.

Fig. 3.5a-b shows the time series of vertical EZ gradients averaged by synoptic node for each scalar, and Fig. 3.5c-d shows the vertical EZ gradients at sunrise grouped by the synoptic node categories. There is a similar distribution over the nodes for the water vapor gradient values, where there are stronger and more variable gradients in water vapor within the low-pressure node. However, the distribution of potential temperature gradients seems to be almost identical between synoptic nodes. Furthermore, plotting the time series mean EZ gradient per synoptic node for both variables (Fig. 3.5a and 3.5b) shows a clear difference in water vapor EZ gradient, and an identical trend in potential temperature EZ gradient between synoptic categories. The synoptic conditions considered in this study appear to have a stronger impact on the EZ gradient for water vapor than

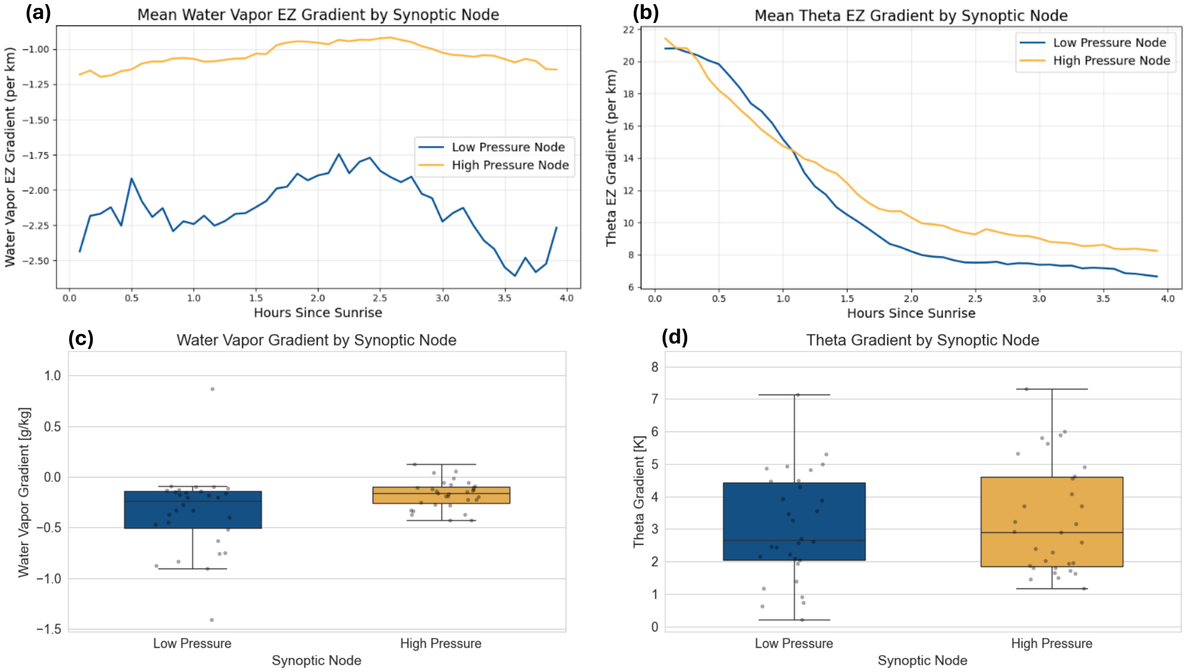

FIGURE 3.5: Time series of the average vertical entrainment zone gradient of (a) water vapor and (c) theta throughout the 4 hour morning window for each synoptic node. Distribution between synoptic nodes of the vertical entrainment zone gradient in (b) water vapor and (d) theta at sunrise time.

for potential temperature. There is strong variance in the potential temperature EZ gradient observed over the cases in this study, however there is no apparent synoptic condition influence on it. Entrainment rates are sensitive to the EZ gradient, and the gradient in water vapor appears to be influenced much more by synoptic conditions. Therefore, EZ gradients must be a key driver to the variability pattern observed in water vapor entrainment, while not meaningfully driving the variability in potential temperature entrainment. EZ gradients are shown to have a close relationship with entrainment, however there are additional factors that need to be considered in the relationship between entrainment variability and atmospheric conditions. Previous studies have shown how surface fluxes are strongly coupled with PBL entrainment by linking it to the amount of surface buoyancy flux (Driedonks 1981; Betts et al. 1992; Angevine et al. 1998), and taking a fraction of the surface flux is a popular way to parameterize entrainment in models (Conzemius and Fedorovich, 2006). Therefore, the role of surface fluxes is important to consider for understanding entrainment rates. Entrainment rates may exert a different relationship to surface fluxes in the morning transition than during the daytime CBL, due to having a shallower CBL and its rising motion in the morning. Furthermore, latent heat flux exerts variability from different environmental conditions. Because of this, the relationship between water vapor entrainment and latent heat flux is more closely examined, as it may also play a role in driving the synoptic variability of water vapor entrainment. Fig. 3.6a shows the regression of water vapor entrainment on the total latent heat flux energy, where a close relationship is observed between dry air entrainment and the measured latent heat flux, with an r value of -0.81 and a slope of -0.95, shown in Fig. 3.6. Here, water vapor entrainment in the morning seems to scale much stronger to latent heat flux than the commonly accepted 0.2 ratio of daytime CBL entrainment to surface buoyancy flux ratio, which is an expected result from past studies (Angevine et al. 2001). There is also a trend in latent heat flux between synoptic nodes showing higher values and variability in the low-pressure node compared to the high-pressure node, shown in Fig. 3.6b. This distribution between nodes is a similar pattern to the original spread of water vapor entrainment between synoptic nodes shown in Fig. 3.3, lending evidence that the variability in latent heat flux is a driver of the synoptic variability pattern of water vapor entrainment.

There is a clear influence of latent heat flux on water vapor entrainment; however, it is

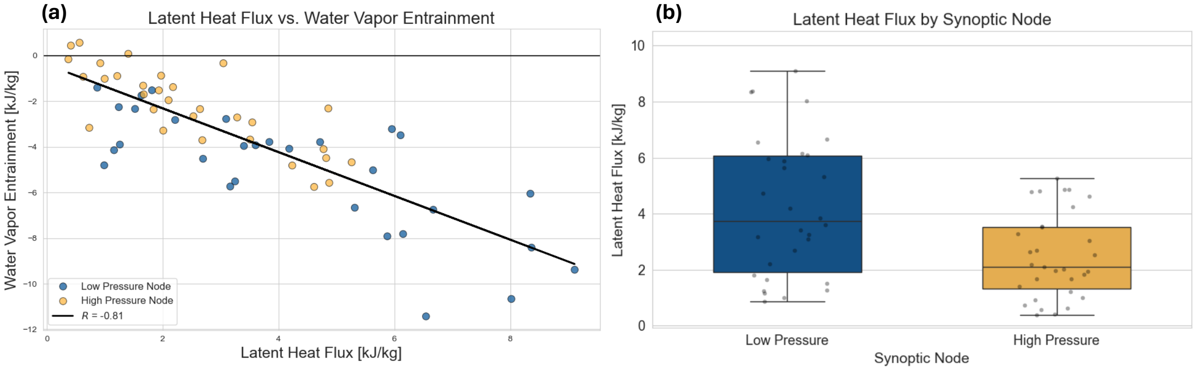

FIGURE 3.6: (a) Water vapor entrainment values regressed onto latent heat flux forcing in the morning transition. (b) The distribution between synoptic nodes of latent heat flux forcing in the morning transition.

important to understand how surface conditions directly related to latent heating themselves correlate with entrainment in the morning transition. Fig. 3.7 displays the results of regressing water vapor entrainment against four surface variables: soil temperature (a), surface pressure (b), surface humidity (c), and surface temperature (d), with synoptic node indicated by color. A consistent increase in entrainment variability is evident under conditions of warmer soils, higher surface temperature and humidity, and lower surface pressure. The physical relationships between these surface variables and entrainment arise from their control on mixed layer growth, thermodynamic contrasts across the EZ, and their correlation with stronger advection patterns. An in depth conversation of these mechanisms is presented in the discussion section. Furthermore, it is clear in Fig. 3.7 that the majority of cases with heightened variability in entrainment are contained within the low-pressure synoptic node. While this study does not isolate all the mechanisms responsible for stronger entrainment variability in low-pressure conditions, these results suggest that surface conditions and synoptic scale dynamics jointly contribute to

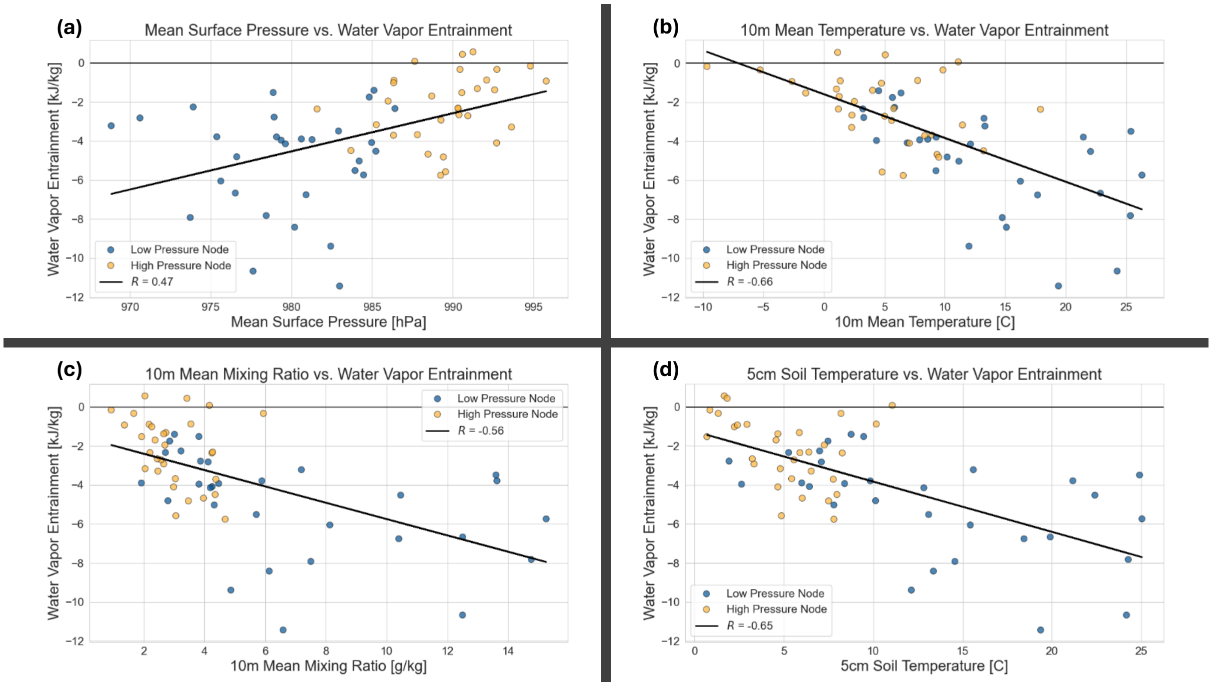

Figure 3.7: Water vapor entrainment values regressed on mean values in the 4 hour morning window for (a) soil temperature (b) surface pressure (c) surface humidity (d) surface temperature. The points are color coded by synoptic node.

the spread of morning transition entrainment.

We have shown the high level factors of EZ gradients, surface fluxes, and surface conditions associated with the difference in the magnitude and variability of entrainment in the morning transition between the synoptic classifications. However, there is more nuance to PBL processes and structure that affect how air is entrained into the PBL in the morning transition that is difficult to view from a high level. Therefore, the rest of this section will make use of case studies to show finer nuances of the boundary layer that may be driving the different entrainment results observed in the synoptic nodes.

3.2 Case Study 1: Role of Residual Layers and Capping Inversions in Morning Entrainment

In this section, two cases are introduced and compared in Fig. 3.8 that had different entrainment results to understand the finer nuances of the morning transition and how they may impact PBL entrainment. The first case considered is on 20 April 2018, from the high-pressure node category. This case showed a relatively weak amount of entrainment, with an energy impact of 0.1 kJ/kg from water vapor and 1.06 kJ/kg from potential temperature entrainment. The other case considered is on 12 July 2019, from the low-pressure synoptic node category. It had greater entrainment, with energy impacts of -10.7 kJ/kg from water vapor and 5.3 kJ/kg from potential temperature entrainment. Comparing these cases will serve as a closer look at the differences between cases of low versus high water vapor entrainment.

Detailed time height cross sections for both cases were created from AERI-derived vertical profiles at the central facility at SGP. These cross sections allow us to see the fine-scale structure of PBL water vapor and temperature for the cases throughout the morning transition. Figure 3.8 shows the cross sections for potential temperature, temperature, and ML-mean standardized water vapor for both cases side by side. An immediate difference in vertical structure can be seen by looking at the potential temperature cross sections. In Fig. 3.8a, there is a pronounced residual layer in the high-pressure node case on the left, resembling an area of vertically uniform potential temperature above the

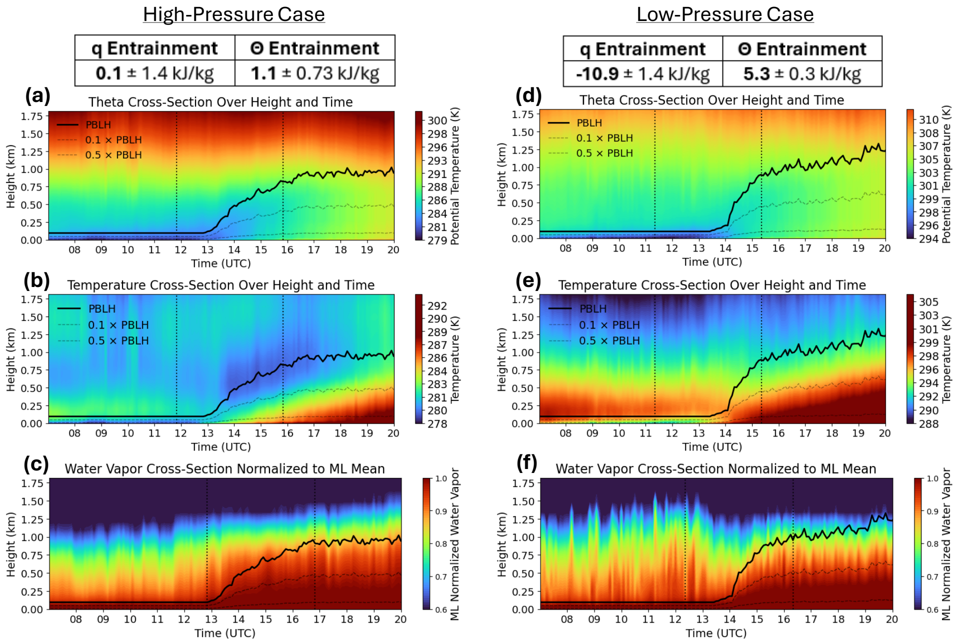

FIGURE 3.8: AERI derived time/height cross sections of theta, temperature, and ML standardized water vapor mixing ratio for a case from the high-pressure node (left) and the low-pressure node (right). Dotted vertical lines indicate the morning transition time window analyzed in this study for both cases.

nocturnal SBL, indicating a layer of well mixed air aloft. This layer persists well into the morning transition through 15 UTC, allowing the PBL to grow through a deeper well-mixed residual layer. The residual layer is also pronounced in the temperature cross section (Fig. 3.8b) where above the nocturnal SBL there is a layer of well mixed, cooler air between 0.5 and 0.75 km. This well-mixed layer is capped by an inversion at 1 km that persists throughout most of the day through 17 UTC.

A similar pattern exists in the cross section of ML-normalized water vapor, shown in Fig. 3.8c, where there is an area of vertically uniform water vapor that the PBL is growing into from 12 to 15 UTC. In the cross sections of the high-pressure case (Fig. 3.8a-c), the result of this residual layer is that the PBL is rising into air of similar thermodynamic properties compared to the mixed layer below. This illustrates how the residual layer in this case has a dampening effect on the amount of entrainment occurring by causing the air aloft that is turbulently mixed and engulfed by the rising PBL to be less dry and warm relative to the ML.

Comparing this to the low-pressure node case on the right in Fig. 3.8d-f, the structure looks different. The residual layer is less vertically uniform in the potential temperature cross section (Fig. 3.8d), with the air above the nocturnal SBL being near 5 K warmer than the mixed layer below. Additionally, the PBL rises faster in height in the low-pressure case from 14 to 15 UTC, rising into and engulfing air aloft more quickly. Consequently, the PBL appears to be rising rapidly into air that is much warmer and dryer than the ML mean in this case, causing entrainment to have a bigger impact on the PBL heat and moisture budgets by nearly 11 kJ/kg and 4 kJ/kg for water vapor and potential temperature entrainment, respectively.

Differences in structure between these two cases can be analyzed by looking at the vertical profiles from radiosonde launches by directly diagnosing the inversions discussed in Fig. 3.8 and showing how synoptic scale conditions can imprint on the structure of the PBL. Radiosondes at SGP were launched every day at approximately 1130 UTC and 1730 UTC, capturing the early morning or nocturnal SBL and daytime CBL, with sunrise times at SGP ranging from 1100 to 1340 UTC, and sunset ranging from 2300 to 0130 (next day) UTC. The results of these radiosonde launches for both cases are displayed in Fig. 3.9. Comparing the profiles for the nocturnal SBL at the 1130 UTC launch, there is an intense inversion present above the SBL at about 900 hPa in the high-pressure node case of about 4 K in strength, whereas there is only a slight inversion aloft in the low-pressure node case higher up at 800 hPa of about 1.5 K. Using the hypsometric equation, the inversion in the high-pressure case has an estimated thickness of 780 m, whereas the low-pressure case inversion has a thickness of about 93 m. A similar comparison can also be made by looking at the daytime CBL profiles from the 1730 UTC launch. The strong inversion aloft remains with a strength of about 4 K at the top of the CBL in the high-pressure node case at the same 900 hPa level. In the daytime CBL profile for the low-pressure node case, there is an inversion present at the top of the CBL, however it is still much weaker compared to the high-pressure case, with a strength of about 2 K.

The stronger inversion in the high-pressure case is associated with the weaker amount of entrainment observed compared to the low-pressure case. The inversion can cause the residual layer in the high-pressure case to persist and stay well-mixed by suppressing vertical mixing and not allowing it to dissipate. Concurrent with the stronger inversion, the high-pressure case experienced a smaller impact from advection of -1.0 and -0.2 kJ/kg for q and θ, compared to 1.9 and -1.3 kJ/kg for q and θ, respectively, in the low-pressure case. The weaker advection may also contribute to the persistence of the residual layer in the high-pressure case by limiting horizontal mixing with air of different properties. Therefore, the reduced amount of advection and the stronger inversion may both more effectively confine the residual layer closer to the surface and allow it to persist longer into the morning transition in the high-pressure node case. Conversely, the weak

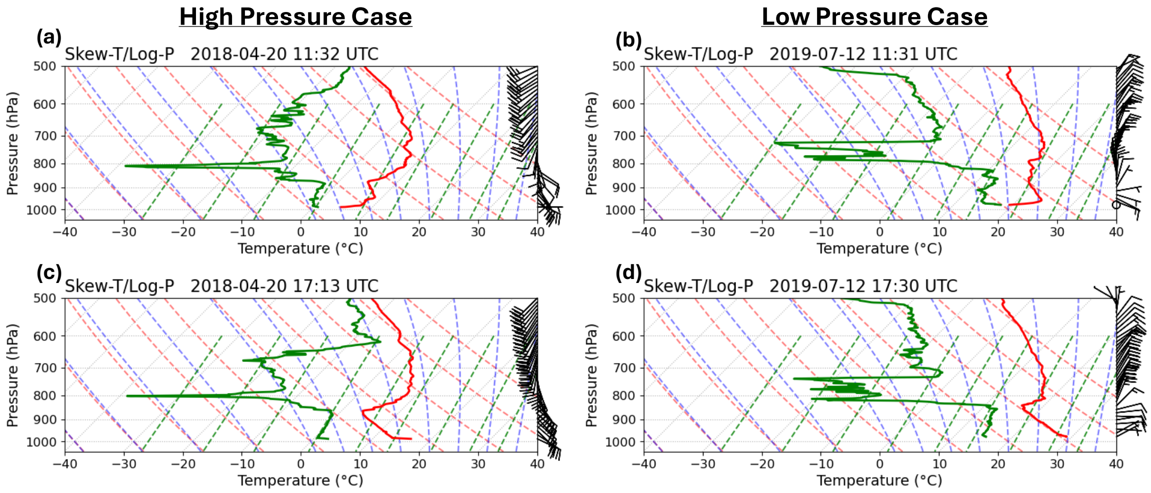

Figure 3.9: Radiosonde profiles of the high-pressure node case (a, c) and the low-pressure node case (b, d) at approximately 11:30 and 17:30 UTC.

inversion in the low-pressure node case can allow the residual layer to erode more quickly, reducing its presence in the morning window.

The presence of the strong inversion aloft in the high-pressure node is a classic signal of the influence of large-scale subsidence. Subsidence is a known complicating issue in understanding entrainment, and here we see an example of how it can affect the structure of the PBL, reducing entrainment in the morning transition. We would expect to see greater large-scale subsidence in high-pressure, anticyclonic conditions (Stull 1988); therefore, large-scale subsidence is likely present in the high-pressure case. This is confirmed in Fig. 3.10, which shows ERA5 data of vertical velocity (ω) and divergence. In the high-pressure case, there is persistent positive vertical velocity throughout most of the troposphere, signifying large-scale sinking motion. Accompanying this vertical motion is consistent positive low-level divergence from 1000 to 800 hPa. Low-level divergence

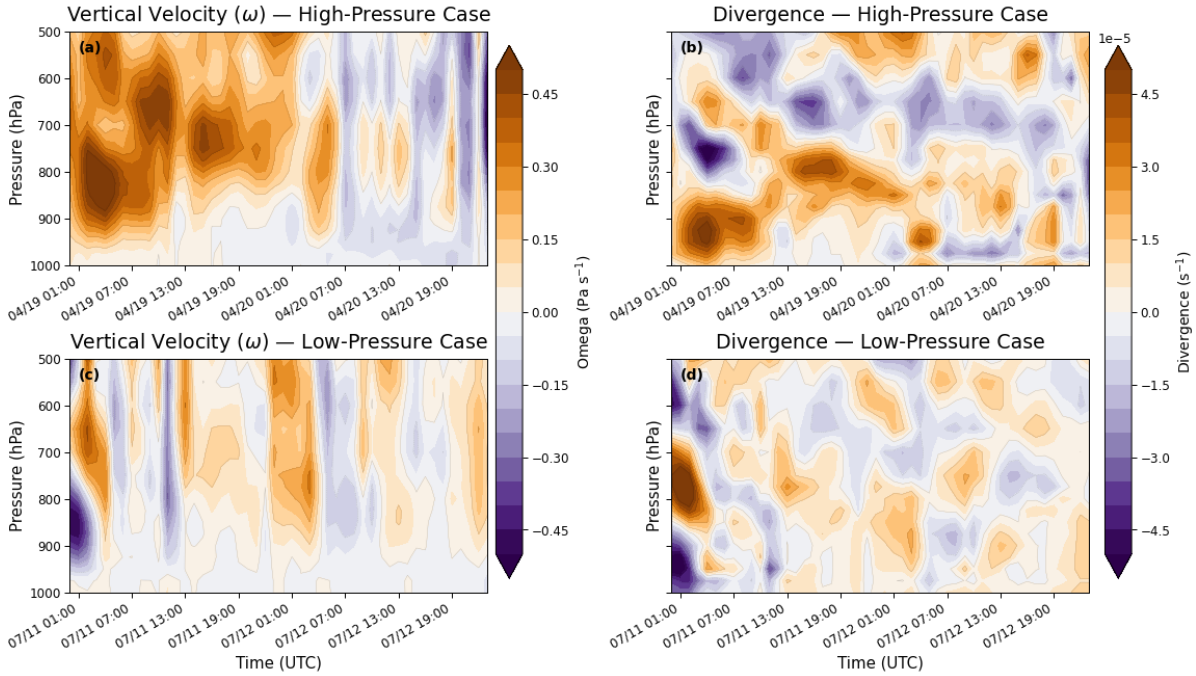

FIGURE 3.10: ERA5 values of vertical velocity (ω) and divergence from surface level to 300 hPa on 19-20 April 2018 (a, b) and 11-12 July 2019 (c, d).

is consistent with large-scale subsidence due to mass continuity of the atmosphere. Together, the vertical velocity and low-level divergence confirm that large-scale subsidence occurred throughout the nighttime before the morning transition on 20 April 2018. In contrast, the low-pressure case on 12 July 2019 shows no consistent trend in vertical velocity or divergence, indicating that large-scale subsidence was not present. The stronger capping inversion, residual layer persistence, and slower CBL growth in the high-pressure case may all result from the large-scale subsidence that occurred the night before the morning transition, leading to a weaker entrainment impact on the mixed layer.

This comparison shows the nuances for how residual layers and large-scale subsidence in the morning transition impact the properties of air being entrained. Discussed in the introduction, Rosenberger et al. (2024) shows how the encroachment term is a substantial piece of the overall forcing in entrainment in the morning transition due to the rising motion of the PBL (Fig. 1.5). This can result in morning entrainment being particularly sensitive to the processes of capping inversions, residual layers, and large-scale subsidence. In return, large-scale subsidence and residual layers appear to be more present in the high-pressure synoptic node cases, and therefore their presence is a further explanation of why we observe weaker and less variable entrainment in these cases compared to the low-pressure node cases.

3.3 Case Study 2: Morning Dependence on large-scale Processes

In this section, the outlier case in water vapor EZ gradient from Fig. 3.4 that had a positive water vapor gradient of 0.8 g/kg at sunrise is examined. This case serves as a good example of how the encroachment term of the PBL morning transition causes entrainment to be sensitive to large-scale processes that would otherwise have little effect during the daytime CBL state. During the daytime CBL, the mixed layer is deep and well mixed, and entrainment occurs along a comparatively steady EZ interface controlled by turbulent mixing of eddies (Stull 1988). In contrast, the morning transition is characterized by rapid boundary layer growth, deepening quickly through the residual layer and engulfing air aloft that may contain thermodynamic anomalies (Blay-Carreras et al. 2014). Because of this rapid growth, entrainment is sensitive to the vertical structure immediately above it, with small differences in elevated moisture or temperature producing large case-to-case variability. The case being considered on 08 July 2018 is a warm day with warm soil, low surface pressure, and a high amount of latent heat flux, presented in table 3.2. Given these conditions, we would expect intense dry air entrainment on this day considering the results from Fig. 3.6 and 3.7, showing how water vapor entrainment scales with these conditions. However, only a moderate amount of drying from entrainment occurred. When looking at the variable with the highest correlation to water vapor entrainment in this study, latent heat flux, this case was expected to have -6.1 kJ/kg of dry air entrainment; however, it only resulted in -3.8 kJ/kg. This case is highlighted in the regression chart in Fig. 3.11.

Mean ML Temperature	Mean ML WV Mixing Ratio	5cm Soil Temperature	Mean Surface Pressure	Total Latent Heat Flux
25.4C	13.6g/kg	24.9C	982hPa	6.1kJ/kg

Table 3.2: Mixed layer and surface conditions, as well as total latent heat flux for the case on 08 July 2018.

An important observation into the source of this unexpected entrainment rate is the positive value of the water vapor gradient around the PBL height at sunrise, 1120 UTC, of 0.8 g/kg. This value is typically negative, as water vapor mixing ratio is expected to decrease through the EZ. Due to this unexpected vertical gradient, the AERI-derived cross section of water vapor is examined for this case to investigate the structure of water vapor throughout the day, shown in Fig. 3.12a. The cross section contains an area of positive water vapor mixing ratio anomaly that appears over the nocturnal SBL starting at 0900 UTC between 0.3 to 1.0 km high. This area of excess moisture persists throughout the night and into the morning, leaving the air aloft to be about 2 g/kg higher in water vapor mixing ratio than the mixed layer in the SBL on average. Consequently,

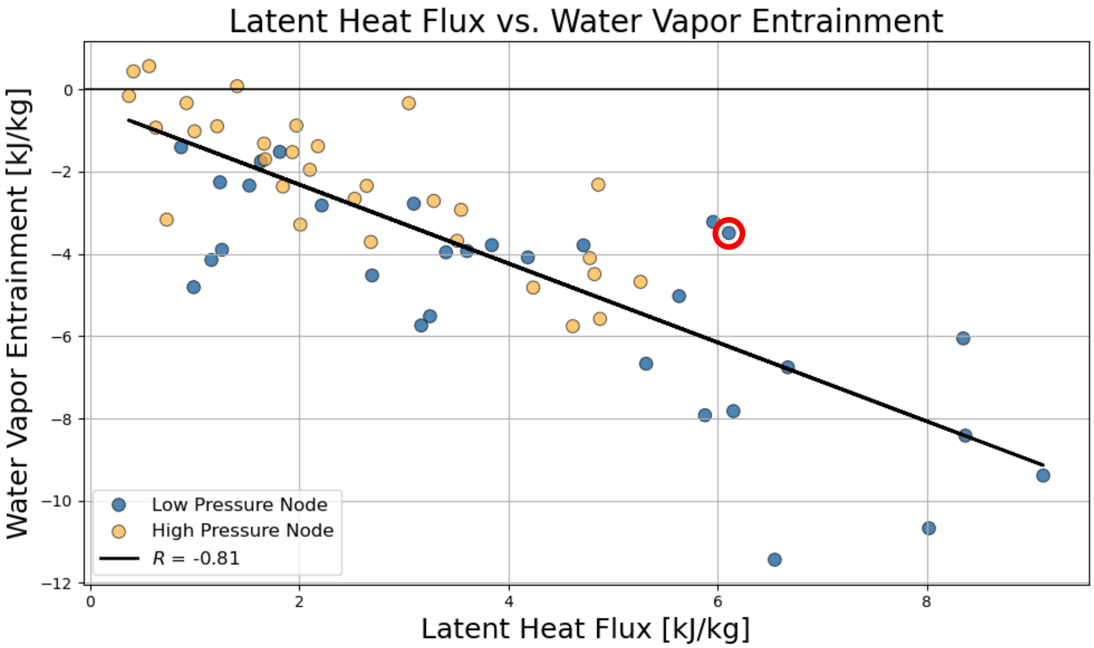

FIGURE 3.11: Water vapor entrainment regressed onto latent heat flux, with the subject of this case study, the case on 08 July 2018, highlighted with a red circle in the plot.

this causes the gradient in water vapor to be positive around sunrise, and results in the morning boundary layer growing into and engulfing this very moist air aloft. This structure can greatly reduce the amount of drying that can occur from the encroachment term of entrainment and is a key driver for the reduced amount drying from entrainment than expected.

The emergence of the area of increased moisture in the cross section (Fig. 3.12a) corresponds closely with the advection rates over the SGP site for this day (Fig. 3.12b). Advection becomes positive around 0800 UTC, indicating the influx of warm, moist air, which is consistent with the timing of the moisture anomaly observed in Fig. 3.12a. Combining the advection observations with the large-scale flow pattern derived from ERA5 data reveals the broader story. There is large-scale transport of warm, moist air from the

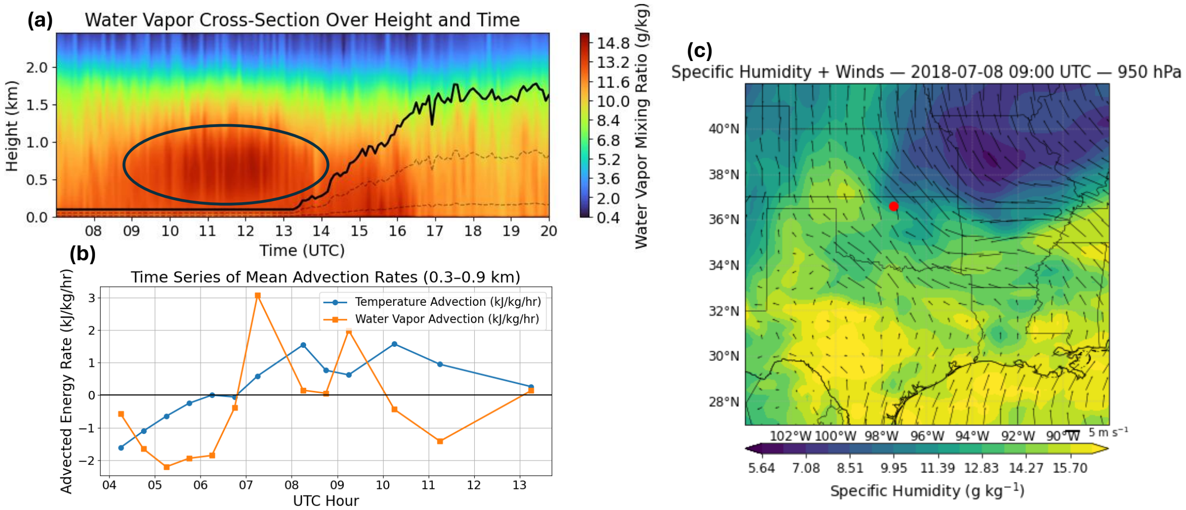

Figure 3.12: (a) AERI derived water vapor time/height cross section, with the sunrise time indicated with a vertical dotted line, (b) advection rate time series during the day of the case over SGP, (c) large-scale horizontal flow pattern and moisture from ERA5 data for the day of the case.

Gulf of Mexico that is making its way over to SGP, causing the area of intense moisture to appear over the SBL in the cross section from Fig. 3.12a. This is a case where the entrainment in the morning transition was impacted by a synoptic scale flow pattern transporting moisture above the boundary layer. The sensitivity of entrainment to synoptic scale flow in this case may be unique to the morning transition, since the growth of the PBL plays a role in engulfing the transported moist air. Referring to Fig. 3.7 where we see a strong increase in variability of entrainment in warm, moist, low-pressure synoptic node cases, the result of this case study presents an explanation to the pattern. These low-pressure node cases are more conducive to enhanced vertical motion and horizontal advection (Holton and Hakim 2013), causing more intense large-scale flow patterns to modulate entrainment rates, adding to the variability.

This example showcases the extra layer of variability in entrainment caused by synoptic scale patterns in addition to the sensitivity to surface fluxes and EZ gradients, and is likely a contributor to the difficulty of accurately modeling entrainment in the morning transition.

3.4 Case Study 3: Intraseasonal Variation by Surface Flux and Gradients

Reviewing the overall results in this study, it is tempting to assume that all the variability in entrainment is due to seasonality. However, there is strong seasonal overlap between the synoptic nodes, shown in figure 3.2, and there is much intraseasonal variability present within the results. This case study presents an example for the intraseasonal variability of entrainment that can occur, dependent on the same factors deemed important for entrainment in this study including vertical EZ gradients, latent heat flux, and mixed layer moisture. Two cases are compared, both days in July 2019 less than two weeks apart. In this section, they will be referred to as Case 1 and Case 2 and are separate from cases in any other section of this study. These cases are very similar to each other in vertical structure, having nearly identical radiosonde profiles at both launch times, occurring right at sunrise around 1130 UTC for these cases, and mid day at 1730 UTC, shown in Fig. 3.13. However, the cases resulted in notably different amounts of total

	Theta Entrainment (kJ/kg)	WV Entrainment (kJ/kg)	Mean Surface Pressure (hPa)	WV Gradient at Sunrise (g/kg)	Latent Heat Flux (kJ/kg)
Case 1 (7/24)	2.64	-4.53	985	-0.40	2.70
Case 2 (7/12)	5.34	-10.67	977	-0.90	8.01

Table 3.3: Total entrainment, mean surface pressure, WVMR EZ vertical gradient at sunrise, and total latent heating for the cases compared in case study 3.

Case 1 (07/24/2019)

Water Vapor Entrainment	Theta Entrainment
-4.5 ± 1.9 kJ/kg	**1.9** ± 0.6 kJ/kg

Case 2 (07/12/2019)

Water Vapor Entrainment	Theta Entrainment
-10.9 ± 1.4 kJ/kg	**5.3** ± 0.3 kJ/kg

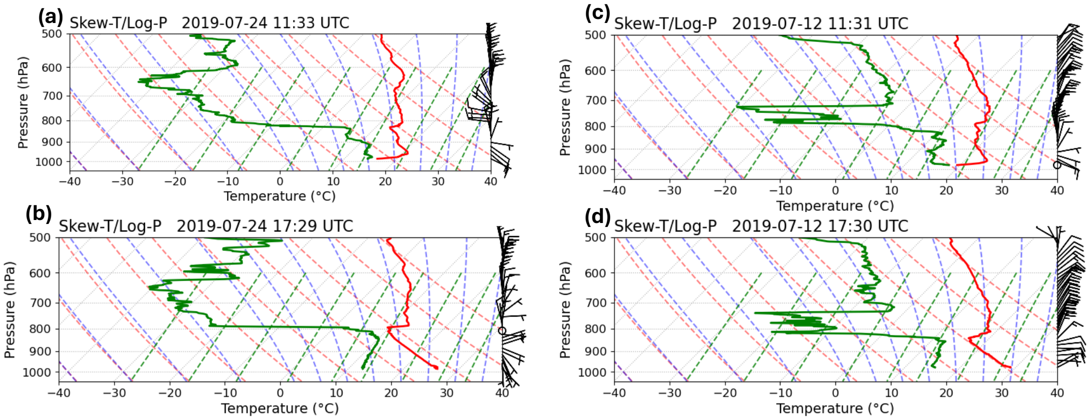

FIGURE 3.13: Radiosonde profiles for the two cases compared in case study 3. The cases show nearly identical vertical profiles at both launch times.

entrainment in the morning transition, shown in table 3.3. Case 1, on July 24, had total entrainment of 2.6 kJ/kg for potential temperature and -4.5 kJ/kg for water vapor entrainment. Case 2, on July 12, had greater total entrainment of 5.3 kJ/kg for potential temperature and -10.7 kJ/kg for water vapor. Despite sharing the same season and having nearly identical vertical structure, entrainment intensity from Case 1 to 2 increased by 104% for potential temperature and 138% for water vapor.Although the cases are identical in structure, they differ in some conditions key to the rate of entrainment in the morning transition. Case 2 had a lower average surface pressure by 8 hPa, stronger latent heating by 5.3 kJ/kg, and a 0.5 g/kg stronger drying gradient in water vapor at sunrise (table 3.3) – all conditions identified in this study that coincide with strong dry air entrainment (Fig 3.3; Fig. 3.4; Fig. 3.6). Both cases follow the trend of water vapor entrainment well based on their latent heat flux, highlighted in Fig. 3.14a. Case 2 had a latent heat flux of 8.0 kJ/kg, 195% greater than Case 1 (2.7 kJ/kg). Looking at the time series of water

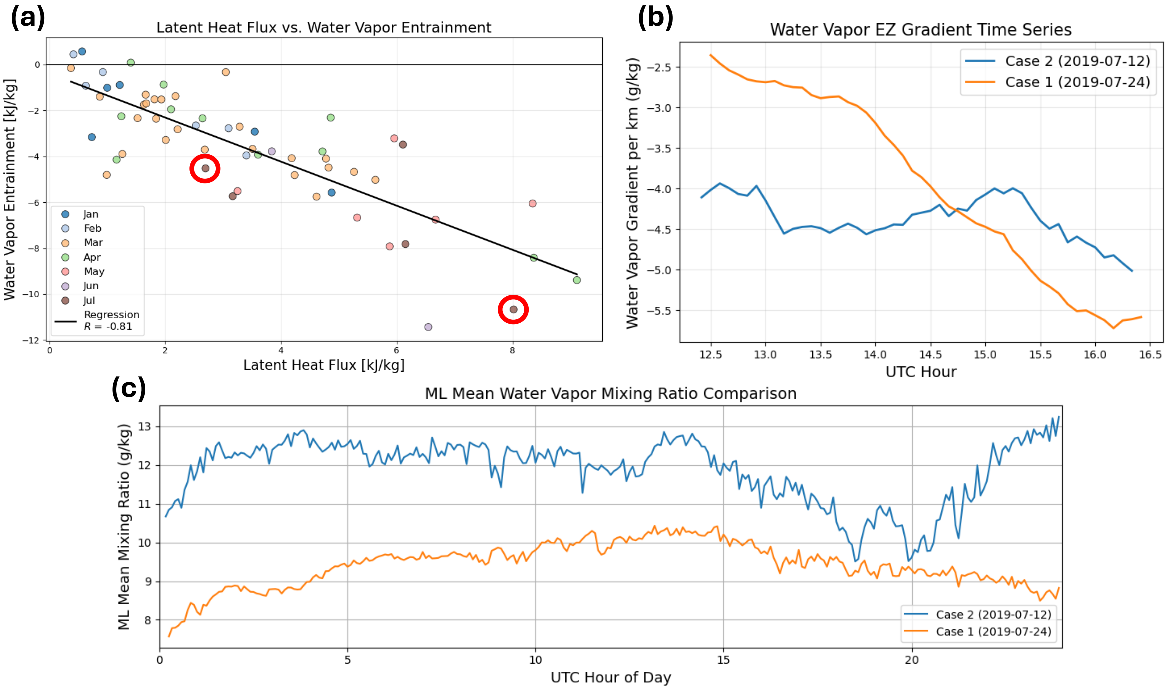

FIGURE 3.14: (a) Water vapor entrainment regressed on latent heat flux, color coded by month, with the two cases in the case study highlighted. (b) Time series of the vertical EZ gradient in water vapor throughout the morning for the two cases, and (c) time series of the mixed layer mean water vapor mixing ratio for both cases.

vapor gradient across the PBL top in Fig. 3.14b, case 2 had a sharper drying gradient by about 60% in the morning hours between 1130 and 1400 UTC compared to case 1, before they eventually become similar and follow the same trend near 1430 UTC and later. Case 2 also presents with a moister mixed layer throughout the day, averaging to be about 20% moister than case 1 in the morning transition. The mixed layer in case 2 remains moister until drying is observed coinciding around the morning transition, resulting in a smaller moisture difference in the daytime CBL.

The combination of these factors in case 2 promotes stronger entrainment because they cause buoyancy production in the mixed layer and thermodynamic contrast across the

PBL top. The substantially larger latent heat flux enhances turbulent kinetic energy production and accelerates mixed-layer growth, increasing entrainment velocity. At the same time, the sharper drying gradient at the PBL top directly amplifies the impact of the entrainment flux. Because case 2 begins with a moister mixed layer, the contrast with the dryer air aloft remains large during the early growth, intensifying the drying effect. The lower surface pressure may further indicate reduced subsidence and a weaker inversion strength, allowing quicker erosion of the stable layer and more vertical motion. Together, these factors in case 2 act synergistically to produce stronger dry air entrainment than a case just twelve days prior in the same season.

These two cases are close together in the same season, yet they vary greatly in the conditions driving entrainment intensity in the morning transition. This shows how the environmental factors key to morning entrainment can have strong intraseasonal variability, which in return causes intraseasonal variability in PBL morning entrainment itself. Therefore, to best understand clear air entrainment in the PBL morning transition, intraseasonal variability must be considered, with surface conditions, mixed layer properties, and vertical gradients as driving factors.

Chapter 4

Discussion

4.1 Energetic Dominance of Water Vapor in Morning PBL Entrainment

One of the most robust findings in this study is that the variability in total ML energy change caused by entrainment in the morning transition is dominated by water vapor rather than potential temperature. Although both scalars contribute to the heat and moisture budgets, water vapor exhibits substantially greater synoptic variability. This result is consistent with the formulations of moist static energy, where water vapor is weighed by the latent heat of vaporization. Therefore, even modest changes in mixing ratio will produce stronger energetic impacts on the ML compared to similar variations in potential temperature.

Coupling the energetic dominance of water vapor in moist static energy, tropospheric water vapor mixing ratio itself is shown to have higher synoptic variability than potential temperature. El Nino Southern Oscillation (ENSO) is a climate variability pattern that plays an outsized role in the synoptic weather patterns over the southern Great Plains, including the ARM SGP site where this study takes place (Ropelewski and Halpert 1986). Johnson et al. (2022) used GNSS-RO to retrieve lower tropospheric moisture and temperature and analyzed the correlation of the zonal mean of each to the ENSO Oceanic Nino Index. They found that specific humidity anomalies associated with ENSO are on the order of ±15% in the lower troposphere, while temperature anomalies are on the order of ±1-2 K. In case study 2, we showed how water vapor anomalies in the lower troposphere can have a control on the amount of dry air entrainment that occurs in the morning transition. Therefore, the energetic dominance of water vapor in PBL entrainment synoptic variability may be a signature of the higher sensitivity of water vapor anomalies to ENSO, the prominent climate variability pattern affecting synoptic conditions over the site at ARM SGP.

4.2 Synoptic Variability and Model Bias

A key result of this study is that entrainment variability differs substantially between the two synoptic nodes produced, with the low-pressure synoptic node exhibiting stronger rates of entrainment and a larger variability in entrainment between cases. Stouffer et al. (2025) documented regional differences in EZ thickness across the United States, using Dual-Polarization Radar to observe its structure. The monthly median EZ thickness varied by 60% in relative thickness to the total depth of the PBL in the morning between regions which have different synoptic patterns and environmental conditions. It is well known in literature that EZ thickness is dynamically linked to entrainment velocity in the PBL; increased turbulence and shear tend to broaden the EZ, allowing deeper penetration of eddies and enhancing the flux of scalars across the inversion (Deardorff 1974; Sullivan et al. 1998; Fedorovich et al. 2004).

The results of synoptic variability of entrainment in this study and that of EZ thickness in Stouffer et al. provide great context for the findings in Banks et al. (2016). Their work has demonstrated that boundary layer parameterization bias in numerical weather prediction models depends on synoptic regime. They showed that WRF model bias under different PBL schemes varies with large-scale synoptic flow patterns found at different sites, particularly during the transition periods of the boundary layer diurnal cycle. Entrainment has been shown to be a key driver for model bias (Angevine et al. 2020). Therefore, the variability of EZ thickness and entrainment forcing might be a key underlying mechanism for the substantially different model bias found in different synoptic regimes, as variations in observed entrainment forcing can cause variation in model bias. Therefore, to improve model bias, it may be worth the effort to include synoptic scale pressure and flow patterns when parameterizing the entrainment forcing in PBL schemes.

Another key result in this study is the larger variance in entrainment rates observed under certain surface conditions, highlighted in Fig. 3.6. These conditions include warm soils, high surface humidity and temperature, and low pressure. This result can be explained with knowledge from past literature. Warmer soils and higher surface temperatures enhance surface sensible heating after sunrise, accelerating the growth of the PBL (Stull 1988). Faster deepening increases the sensitivity of entrainment to inversion strength and to vertical thermodynamic gradients across the EZ (Tennekes 1973; Deardorff 1974; Tennekes and Driedonks 1981). Higher surface humidity strengthens the vertical moisture contrast between the mixed layer and the drier free troposphere, resulting in smaller changes in entrainment rates producing larger impacts on the ML moisture budget (Betts 1973; Angevine et al. 2001; Henkes et al. 2021). Lower surface pressure is associated with enhanced vertical motion and horizontal advection (Holton and Hakim 2013), which can increase variability in morning PBL entrainment. Together, the stronger surface forcings and stronger synoptic flow help to explain the larger spread in morning entrainment rates observed in the low-pressure node cases. This also provides important context for the difference in model bias observed between different sites in Banks et al. (2016).

4.3 Residual Layers and Subsidence

Large-scale subsidence emerges as an important factor modulating entrainment in the high-pressure synoptic node. Subsidence is commonly associated with anticyclones and persistent high-pressure systems (Stull 1988), which are characterized by the high-pressure node in this study. Downward velocity warms and dries the air aloft through adiabatic compression, strengthening capping inversions and stabilizing the EZ. A typical radiosonde profile during the presence of large-scale subsidence will show an enhanced inversion aloft in the atmosphere due to subsidence-induced warming (Angevine et al.

1998). Because entrainment parameterizations often struggle to represent externally forced inversion strengthening (Conzemius and Fedorovich 2006), subsidence has long been recognized as a complicating factor in entrainment dynamics and model performance (vanZanten et al. 1999; Blay-Carreras et al. 2014).

In the first case study, section 3.2, an example of subsidence coinciding with weaker entrainment was observed. A stronger inversion in the high-pressure case was present in Fig. 3.8, which may play a role in the weaker amount of entrainment observed compared to that of the low-pressure case. The inversion is likely causing the residual layer in the high-pressure case to persist and stay well mixed by suppressing vertical motion and not allowing it to dissipate. Therefore, along with reducing turbulent mixing near the top of the PBL, the inversion more effectively maintains the strength of the residual layer closer to the surface and allows it to persist longer into the morning transition in the high-pressure case. Conversely, the weak inversion in the low-pressure case allows the residual layer to erode quicker, reducing its presence in the morning window. The presence of the strong inversion aloft in the high-pressure node is a classic signal of large-scale subsidence. Subsidence is a known complicating issue to understanding entrainment, and here we see an example of how it is coinciding with a reduced amount of entrainment in the morning transition.

The structure and persistence of the residual layer plays a central role in the morning transition and throughout the rest of the day. Blay-Carreras et al. (2014) studied the effects of residual layer structure using observations from the BLLAST field campaign and LES modeling. They found that residual layer structure controls the growth of the PBL in the morning transition through its modulation of entrainment. They show that if the residual layer is strongly stratified and contains a strong inversion, entrainment in the morning transition is reduced and the PBL grows slower. They found that particularly when a strong residual layer coincides with subsidence, as in the weak entrainment case from the first case study (section 3.2), entrainment is particularly weak. Furthermore, stronger residual layers may be more present and stratified in the winter months, when nocturnal inversions are shallower and the prior day's mixed layer becomes more effectively decoupled from the surface. Weaker morning heating in winter slows erosion of the stable boundary layer, allowing the residual layer to persist well into the late morning. In addition, a weaker Great Plains low-level jet during winter can reduce shear-driven mixing overnight, helping preserve residual layers in a stratified structure. Therefore, the weaker amount of entrainment observed in the high-pressure node may contain signal from the presence of stronger, stratified residual layers, due to the high-pressure node containing more cases from winter months.

Observational studies further highlight the importance of residual-layer moisture in controlling daytime convective evolution. Henkes et al. (2021), a dry-season observational study in the central Amazon, demonstrated that the depth and water vapor structure of the residual layer strongly influences the convective potential of the day. They found that entrained moisture from the residual layer is often decisive in determining whether the PBL acquires sufficient moist static energy to overcome convective inhibition. Days featuring a moist residual layer above the nocturnal stable boundary layer were more likely to develop deep convection. Although Henkes et al. focuses on the tropics, a similar mechanism may operate in the Southern Great Plains: deeper and moister morning residual layers lead to moister air being entrained into the growing mixed layer, thereby increasing morning PBL moisture and enhancing downstream convective development.

4.4 Surface Fluxes and the Entrainment Ratio

Entrainment in convective boundary layer theory and PBL modeling is commonly parameterized as a fixed fraction of the surface buoyancy flux. Mixed-layer scaling arguments and numerous field studies discussed in section 1.3 of the introduction have suggested that the entrainment buoyancy flux is approximately 20% of the surface buoyancy flux, yielding an entrainment-to-surface flux ratio near 0.2 under idealized daytime conditions. This assumption has been widely adopted for entrainment parameterization in PBL model schemes. However, there is doubt whether this holds true in a real world boundary layer where subsidence and vertical wind shear can complicate entrainment rates (Wulfmeyer 1999a). Increasing observational and large-eddy simulation (LES) evidence suggests that this ratio is not universal and may vary substantially depending on boundary-layer structure and environmental conditions.

Conzemius and Fedorovich (2006) examined the relationship between entrainment and surface forcing in LES simulations of a sheared convective boundary layer. Their results cast doubt on the robustness of the 0.2 ratio value, particularly in the presence of entrainment-zone shear. They demonstrated that shear across the inversion enhances turbulent kinetic energy production near the PBL top, increasing entrainment efficiency beyond what is predicted by surface buoyancy flux scaling alone. Most notably for this study, their simulations showed substantially larger entrainment-to-surface flux ratios during the morning transition, when the boundary layer is rapidly deepening. In some cases, the entrainment flux approached or exceeded the magnitude of the surface flux (ratios near or above 1), highlighting that CBL development in the morning transition may fundamentally depart from steady-state assumptions. Similarly, Angevine et al. (2001) noted that during the morning transition under idealized conditions, the ratio of entrainment to surface flux is expected to be much higher. This difference in ratio to surface flux in the morning transition may in part be due to the encroachment term of entrainment from the rising motion of the morning PBL.

The results of the present study are consistent with this perspective. When water vapor entrainment is regressed against the corresponding surface latent heat flux, the inferred entrainment-to-surface flux ratio is substantially larger than 0.2. The regression slope is near 0.9 (Fig. 3.6a), indicating that water vapor entrainment is much greater than 20% of the corresponding latent heat flux during the morning transition. Although this is only considering water vapor flux instead of total buoyancy flux, this magnitude may be far greater than what would be predicted under classical steady state CBL scaling. This enhanced ratio is consistent with the rapid deepening of the mixed layer after sunrise. During the morning transition, boundary-layer growth is characterized by engulfment of the residual layer and strong gradients in moisture across the inversion. Therefore, entrainment is not simply a response to surface flux; instead, it reflects the combined effects of surface buoyancy production, inversion strength, subsidence, and shear at the PBL top. Because the inversion contains substantial contrasts in moisture, even small increases in mixed-layer depth can produce large entrainment fluxes relative to the surface forcing.

These findings suggest that parameterizations relying on a fixed entrainment-to-surface buoyancy flux ratio may be inadequate for representing morning transition dynamics. A larger, time-dependent ratio, or a scheme that incorporates inversion strength, subsidence, and shear may be necessary to accurately capture entrainment during the rapid boundary-layer growth in the morning transition. This has implications for model bias in the early daytime hours, when inaccurate representation of entrainment can lead to systematic errors in mixed-layer depth, moisture, and temperature, causing inaccurate forecasts of daytime convection and storm development.

Chapter 5

Summary and Conclusions

5.1 Results Summary

This study aimed to quantify and address research questions regarding the variability and physical controls of PBL clear air entrainment forcing during the morning transition using a remote sensing based budget closure method using mixing diagrams. By leveraging cutting-edge instruments at SGP to observe continuous, high resolution profiles of the lower troposphere, advances in measuring advection from Wagner et al. (2022), and a mixing diagram method proven in Wakefield et al. (2023), a first-of-its-kind dataset of morning entrainment observations was produced.

The mixing diagram method was successfully applied to the morning transition, resulting in a dataset of 61 entrainment morning transition forcing observations. Strict case selection criteria were implemented to ensure reasonable uncertainty in the entrainment estimates, particularly by limiting the presence of clouds, precipitation, and synoptic fronts in the final case selections. The resulting dataset spans January through July, with the greatest concentration of cases occurring in March and April.

To address how entrainment varies with synoptic and environmental conditions, cases were categorized using self-organizing maps into higher and lower-pressure regimes. A clear distinction emerged between the two regimes, with a weaker and less variable entrainment forcing in the higher-pressure conditions, and stronger and more variable entrainment forcing in the lower-pressure conditions. This variability pattern in entrainment between synoptic regimes is present in both water vapor and potential temperature entrainment; however water vapor shows to be the dominant mode of energetic variability in entrainment between the synoptic regimes.

The results further demonstrate that entrainment during the morning transition is closely related to surface fluxes, particularly with water vapor entrainment and latent heating. Vertical gradients of temperature and moisture across the entrainment zone were also identified as key drivers of the variability in entrainment between synoptic conditions. Stronger EZ drying gradients in water vapor mixing ratio were observed in the lower-pressure conditions, coinciding with enhanced drying of the mixed layer due to entrainment. Furthermore, the variability in entrainment observed in this study showed behavior of both seasonal and intraseasonal variability, with both modes of variability coinciding with variability in EZ gradients and surface fluxes.

Through case studies, processes unique to the morning transition were shown to play a formative role in the impact of entrainment. During this transition, the rapid growth of the CBL makes entrainment sensitive to the layer of air it is growing into. We have shown how this encroachment process can make entrainment rates sensitive to large-scale transport of moisture impacting the air aloft of the nocturnal SBL. We also showed how the structure and persistence of the residual layer, along with the rate of growth of the PBL have a strong control on the impact of entrainment in the morning transition. Furthermore, we demonstrate how these factors are shaped and influenced by the nocturnal capping inversion and large-scale subsidence processes of the nocturnal SBL.

5.2 Motivation for Future Work

The results of this study provide a strong observational foundation for understanding entrainment during the morning transition, while also highlighting several avenues for future work. First, applying this method to other locations that have different land cover, climate, and synoptic flow patterns would provide more comprehensive insight into how entrainment behaves and interacts with atmospheric and environmental processes. The Bankhead National Forest ARM site would be a logical place to apply this method next, as it already has the instruments and measurement capabilities to do it. Next, increasing the case count and the number of self-organizing map nodes along with it may enable a more refined analysis of the morning entrainment forcing by isolating finer nuances of the variability.

Another key area for future work motivated by this study is improving the representation of the encroachment term of entrainment in models. This study demonstrates how the encroachment in the morning transition can cause entrainment to behave much differently than how it does in classic entrainment theory, which is based off PBL steady state turbulent mixing. Observations from applying this method can be used to test against model output and help refine the parameterization of entrainment in the morning transition.

More research is also needed to understand the relationship between morning entrainment forcing and daytime conditions. In particular, understanding how entrainment in the morning transition influences daytime convection, storm development, and precipitation would provide valuable information on land-atmosphere feedback and severe weather forecasting. Finally, Wulfmeyer et al. (2016) presents a method to directly forecast and understand PBL entrainment by relating it to the higher-order moments of meteorological variables in the boundary layer. The quantification of entrainment using the method in this study can provide observational values to test against the relationships to higher-order moments proposed in Wulfmeyer et al. (2016). The application to this may be essential for advancing the predictive understanding of boundary layer processes.

Bibliography

Andersen, T. K., D. E. Radcliffe, and J. M. Shepherd, 2013: Quantifying Surface Energy Fluxes in the Vicinity of Inland-Tracking Tropical Cyclones. *Journal of Applied Meteorology and Climatology*, **52**, 2797–2808, doi:10.1175/JAMC-D-13-035.1.
URL `https://journals.ametsoc.org/view/journals/apme/52/12/jamc-d-13-035.1.xml`

Angevine, 1999: Entrainment results including advection and case studies from the Flatland boundary layer experiments. *Journal of Geophysical Research: Atmospheres*, **104**, 30947–30963, doi:10.1029/1999JD900930.
URL `https://agupubs.onlinelibrary.wiley.com/doi/10.1029/1999JD900930`

Angevine, W. M., 2008a: Transitional, entraining, cloudy, and coastal boundary layers. *Acta Geophysica, 56, 2-20 doi:10.2478/s11600-11007-10035-11601*, doi:10.2478/s11600-11007-10035-11601.

— 2008b: Transitional, entraining, cloudy, and coastal boundary layers. *Acta Geophysica*, **56**, 2–20, doi:10.2478/s11600-007-0035-1.
URL `http://link.springer.com/10.2478/s11600-007-0035-1`

Angevine, W. M., H. K. Baltink, and F. C. Bosveld, 2001: Observations Of The Morning Transition Of The Convective Boundary Layer. *Boundary-Layer Meteorology*, **101**, 209–227, doi:10.1023/A:1019264716195.
URL `https://link.springer.com/10.1023/A:1019264716195`

Angevine, W. M., A. W. Grimsdell, L. M. Hartten, and A. C. Delany, 1998: The Flatland Boundary Layer Experiments. *Bulletin of the American Meteorological Society*, **79**, 419–431, doi:10.1175/1520-0477(1998)079¡0419:TFBLE¿2.0.CO;2.
URL `http://journals.ametsoc.org/doi/10.1175/1520-0477(1998)079<0419:TFBLE>2.0.CO;2`

Arndt, D. S., J. B. Basara, R. A. McPherson, B. G. Illston, G. D. McManus, and D. B. Demko, 2009: Observations of the Overland Reintensification of Tropical Storm Erin (2007). *Bulletin of the American Meteorological Society*, **90**, 1079–1094, doi:10.1175/2009BAMS2644.1.
URL `https://journals.ametsoc.org/doi/10.1175/2009BAMS2644.1`

Ayotte, K. W., P. P. Sullivan, A. Andron, S. C. Doney, A. A. M. Holtslag, W. G. Large, J. C. McWilliams, C.-H. Moeng, M. J. Otte, J. J. Tribbia, and J. C. Wyngaard, 1996: An evaluation of neutral and convective planetary boundary-layer parameterizations relative to large eddy simulations. *Boundary-Layer Meteorology*, **79**, 131–175, doi:10.1007/BF00120078.
URL `http://link.springer.com/10.1007/BF00120078`

Baidar, S., T. J. Wagner, D. D. Turner, and W. A. Brewer, 2023: Using optimal estimation to retrieve winds from velocity-azimuth display (VAD) scans by a Doppler lidar. *Atmospheric Measurement Techniques*, **16**, 3715–3726, doi:10.5194/amt-16-3715-2023. URL `https://amt.copernicus.org/articles/16/3715/2023/`

Banks, R. F., J. Tiana-Alsina, J. M. Baldasano, F. Rocadenbosch, A. Papayannis, S. Solomos, and C. G. Tzanis, 2016: Sensitivity of boundary-layer variables to PBL schemes in the WRF model based on surface meteorological observations, lidar, and radiosondes during the HygrA-CD campaign. *Atmospheric Research*, **176-177**, 185–201, doi:10.1016/j.atmosres.2016.02.024.

URL `https://linkinghub.elsevier.com/retrieve/pii/S0169809516300412`

Barr, A. G. and A. K. Betts, 1997: Radiosonde boundary layer budgets above a boreal forest. *Journal of Geophysical Research: Atmospheres*, **102**, 29205–29212, doi:10.1029/97JD01105.

URL `https://agupubs.onlinelibrary.wiley.com/doi/10.1029/97JD01105`

Bauer, H., F. Späth, D. Lange, R. Thundathil, J. Ingwersen, A. Behrendt, and V. Wulfmeyer, 2023: Evolution of the Convective Boundary Layer in a WRF Simulation Nested Down to 100 m Resolution During a Cloud-Free Case of LAFE, 2017 and Comparison to Observations. *Journal of Geophysical Research: Atmospheres*, **128**, e2022JD037212, doi:10.1029/2022JD037212.

URL `https://agupubs.onlinelibrary.wiley.com/doi/10.1029/2022JD037212`

Benson, D. O. and P. A. Dirmeyer, 2021: Characterizing the Relationship between Temperature and Soil Moisture Extremes and Their Role in the Exacerbation of Heat Waves over the Contiguous United States. *Journal of Climate*, **34**, 2175–2187, doi:10.1175/JCLI-D-20-0440.1.

URL `https://journals.ametsoc.org/view/journals/clim/34/6/JCLI-D-20-0440.1.xml`

Betts, A. K., 1984: Boundary Layer Thermodynamics of a High Plains Severe Storm. *Monthly Weather Review*, **112**, 2199–2211, doi:10.1175/1520-0493(1984)112¡2199:BLTOAH¿2.0.CO;2.

URL `http://journals.ametsoc.org/doi/10.1175/1520-0493(1984)112<2199:BLTOAH>2.0.CO;2`

— 1992: FIFE atmospheric boundary layer budget methods. *Journal of Geophysical Research: Atmospheres*, **97**, 18523–18531, doi:10.1029/91JD03172.

URL `https://agupubs.onlinelibrary.wiley.com/doi/10.1029/91JD03172`

Betts, A. K. and A. G. Barr, 1996: First International Satellite Land Surface Climatology Field Experiment 1987 sonde budget revisited. *Journal of Geophysical Research: Atmospheres*, **101**, 23285–23288, doi:10.1029/96JD02247.

URL `https://agupubs.onlinelibrary.wiley.com/doi/10.1029/96JD02247`

Betts, A. K., R. L. Desjardins, and J. I. MacPherson, 1992: Budget analysis of the boundary layer grid flights during FIFE 1987. *Journal of Geophysical Research: Atmospheres*,

97, 18533–18546, doi:10.1029/91JD03173.

URL `https://agupubs.onlinelibrary.wiley.com/doi/10.1029/91JD03173`

Betts, A. K., R. L. Desjardins, J. I. Macpherson, and R. D. Kelly, 1990: Boundary-layer heat and moisture budgets from fife. *Boundary-Layer Meteorology*, **50**, 109–138, doi:10.1007/BF00120520.

URL `http://link.springer.com/10.1007/BF00120520`

Blackadar, A. K., 1957: Boundary Layer Wind Maxima and Their Significance for the Growth of Nocturnal Inversions. *Bulletin of the American Meteorological Society*, **38**, 283–290, doi:10.1175/1520-0477-38.5.283.

URL `https://journals.ametsoc.org/doi/10.1175/1520-0477-38.5.283`

Blay-Carreras, E., D. Pino, J. Vilà-Guerau De Arellano, A. Van De Boer, O. De Coster, C. Darbieu, O. Hartogensis, F. Lohou, M. Lothon, and H. Pietersen, 2014: Role of the residual layer and large-scale subsidence on the development and evolution of the convective boundary layer. *Atmospheric Chemistry and Physics*, **14**, 4515–4530, doi:10.5194/acp-14-4515-2014.

URL `https://acp.copernicus.org/articles/14/4515/2014/`

Blumberg, W. G., T. J. Wagner, D. D. Turner, and J. Correia, 2017: Quantifying the Accuracy and Uncertainty of Diurnal Thermodynamic Profiles and Convection Indices Derived from the Atmospheric Emitted Radiance Interferometer. *Journal of Applied Meteorology and Climatology*, **56**, 2747–2766, doi:10.1175/JAMC-D-17-0036.1.

URL `https://journals.ametsoc.org/view/journals/apme/56/10/jamc-d-17-0036.1.xml`

Cohen, A. E., S. M. Cavallo, M. C. Coniglio, and H. E. Brooks, 2015: A Review of Planetary Boundary Layer Parameterization Schemes and Their Sensitivity in Simulating Southeastern U.S. Cold Season Severe Weather Environments. *Weather and Forecasting*, **30**, 591–612, doi:10.1175/WAF-D-14-00105.1.

URL `https://journals.ametsoc.org/view/journals/wefo/30/3/waf-d-14-00105_1.xml`

Conzemius, R. J. and E. Fedorovich, 2006: Dynamics of Sheared Convective Boundary Layer Entrainment. Part I: Methodological Background and Large-Eddy Simulations. *Journal of the Atmospheric Sciences*, **63**, 1151–1178, doi:10.1175/JAS3691.1.

URL `https://journals.ametsoc.org/doi/10.1175/JAS3691.1`

Cook, D. R. and R. C. Sullivan, 2020: Eddy correlation flux measurement system (ECOR) instrument handbook. Technical report, ARM Tech. Rep. DOE/SC-ARM-TR-052, 24 pp.

URL `https://www.arm.gov/publications/tech_reports/handbooks/ecor_handbook.pdf`

Cooper, D. I. and W. E. Eichinger, 1994: Structure of the atmosphere in an urban planetary boundary layer from lidar and radiosonde observations. *Journal of Geophysical Research: Atmospheres*, **99**, 22937–22948, doi:10.1029/94JD01944.

URL `https://agupubs.onlinelibrary.wiley.com/doi/10.1029/94JD01944`

Crook, N. A., 1996: Sensitivity of Moist Convection Forced by Boundary Layer Processes to Low-Level Thermodynamic Fields. *Monthly Weather Review*, **124**, 1767–1785, doi:10.1175/1520-0493(1996)124¡1767:SOMCFB¿2.0.CO;2.
URL `http://journals.ametsoc.org/doi/10.1175/1520-0493(1996)124<1767:SOMCFB>2.0.CO;2`

Crum, T. D., R. B. Stull, and E. W. Eloranta, 1987: Coincident Lidar and Aircraft Observations of Entrainment into Thermals and Mixed Layers. *Journal of Climate and Applied Meteorology*, **26**, 774–788, doi:10.1175/1520-0450(1987)026¡0774:CLAAOO¿2.0.CO;2.
URL `http://journals.ametsoc.org/doi/10.1175/1520-0450(1987)026<0774:CLAAOO>2.0.CO;2`

Dabberdt, W. F., M. A. Carroll, D. Baumgardner, G. Carmichael, R. Cohen, T. Dye, J. Ellis, G. Grell, S. Grimmond, S. Hanna, J. Irwin, B. Lamb, S. Madronich, J. McQueen, J. Meagher, T. Odman, J. Pleim, H. P. Schmid, and D. L. Westphal, 2004: Meteorological Research Needs for Improved Air Quality Forecasting: Report of the 11th Prospectus Development Team of the U.S. Weather Research Program*. *Bulletin of the American Meteorological Society*, **85**, 563–586, doi:10.1175/BAMS-85-4-563.
URL `https://journals.ametsoc.org/view/journals/bams/85/4/bams-85-4-563.xml`

Davis, K., D. Lenschow, C. Kiemle, G. Ehret, A. Giez, and J. Mann, 1997: The Role of Entrainment in Surface-Atmosphere Interactions over the Boreal Forest. *Journal of*

Geophysical Research. 102. 219-230. 10.1029/97JD02236, doi:10.1029/97JD02236.

De Arellano, J. V., B. Gioli, F. Miglietta, H. J. J. Jonker, H. K. Baltink, R. W. A. Hutjes, and A. A. M. Holtslag, 2004: Entrainment process of carbon dioxide in the atmospheric boundary layer. *Journal of Geophysical Research: Atmospheres*, **109**, 2004JD004725, doi:10.1029/2004JD004725.
URL `https://agupubs.onlinelibrary.wiley.com/doi/10.1029/2004JD004725`

Deardorff, J. W., 1974: Three-dimensional numerical study of the height and mean structure of a heated planetary boundary layer. *Boundary-Layer Meteorology*, **7**, 81–106, doi:10.1007/BF00224974.
URL `http://link.springer.com/10.1007/BF00224974`

Driedonks, A. G. M., 1982: Models and observations of the growth of the atmospheric boundary layer. *Boundary-Layer Meteorology*, **23**, 283–306, doi:10.1007/BF00121117.
URL `http://link.springer.com/10.1007/BF00121117`

Driedonks, A. G. M. and H. Tennekes, 1984: Entrainment Effects in the Well-Mixed Atmospheric Boundary Layer. *Boundary Layer Structure*, H. Kaplan and N. Dinar, eds., Springer Netherlands, Dordrecht, 75–105.
URL `http://link.springer.com/10.1007/978-94-009-6514-0_4`

Emanuel, K., J. Callaghan, and P. Otto, 2008: A Hypothesis for the Redevelopment of Warm-Core Cyclones over Northern Australia. *Monthly Weather Review*, **136**, 3863–3872, doi:10.1175/2008MWR2409.1.
URL `https://journals.ametsoc.org/doi/10.1175/2008MWR2409.1`

Fabry, F., 2006: The Spatial Variability of Moisture in the Boundary Layer and Its Effect on Convection Initiation: Project-Long Characterization. *Monthly Weather Review*, **134**, 79–91, doi:10.1175/MWR3055.1.
URL `http://journals.ametsoc.org/doi/10.1175/MWR3055.1`

Fedorovich, E., R. Conzemius, and D. Mironov, 2004: Convective Entrainment into a Shear-Free, Linearly Stratified Atmosphere: Bulk Models Reevaluated through Large Eddy Simulations. *Journal of the Atmospheric Sciences*, **61**, 281–295, doi:10.1175/1520-0469(2004)061¡0281:CEIASL¿2.0.CO;2.
URL `http://journals.ametsoc.org/doi/10.1175/1520-0469(2004)061<0281:CEIASL>2.0.CO;2`

Freire, L. S. and N. L. Dias, 2013: Residual layer effects on the modeling of convective boundary layer growth rates with a slab model using FIFE data. *Journal of Geophysical Research: Atmospheres*, **118**, doi:10.1002/jgrd.50796.
URL `https://agupubs.onlinelibrary.wiley.com/doi/10.1002/jgrd.50796`

Fritz, A. M., K. Lapo, A. Freundorfer, T. Linhardt, and C. K. Thomas, 2021: Revealing the Morning Transition in the Mountain Boundary Layer Using Fiber-Optic Distributed Temperature Sensing. *Geophysical Research Letters*, **48**, e2020GL092238, doi:10.1029/2020GL092238.
URL `https://agupubs.onlinelibrary.wiley.com/doi/10.1029/2020GL092238`

Gadde, S. N. and R. J. A. M. Stevens, 2021: Effect of low-level jet height on wind farm performance. *Journal of Renewable and Sustainable Energy*, **13**, 013305, doi:10.1063/5.0026232.

URL `https://pubs.aip.org/jrse/article/13/1/013305/284849/Effect-of-low-level-jet-height-on-wind-farm`

García-Díez, M., J. Fernández, L. Fita, and C. Yagüe, 2013: Seasonal dependence of WRF model biases and sensitivity to PBL schemes over Europe. *Quarterly Journal of the Royal Meteorological Society*, **139**, 501–514, doi:10.1002/qj.1976.

URL `https://rmets.onlinelibrary.wiley.com/doi/10.1002/qj.1976`

Gryning, S. and E. Batchvarova, 1994: Parametrization of the depth of the entrainment zone above the daytime mixed layer. *Quarterly Journal of the Royal Meteorological Society*, **120**, 47–58, doi:10.1002/qj.49712051505.

URL `https://rmets.onlinelibrary.wiley.com/doi/10.1002/qj.49712051505`

Halios, C. H. and J. F. Barlow, 2018: Observations of the Morning Development of the Urban Boundary Layer Over London, UK, Taken During the ACTUAL Project. *Boundary-Layer Meteorology*, **166**, 395–422, doi:10.1007/s10546-017-0300-z.

URL `http://link.springer.com/10.1007/s10546-017-0300-z`

Henkes, A., G. Fisch, L. A. T. Machado, and J.-P. Chaboureau, 2021: Morning boundary layer conditions for shallow to deep convective cloud evolution during the dry season in the central Amazon. *Atmospheric Chemistry and Physics*, **21**, 13207–13225, doi:10.5194/acp-21-13207-2021.

URL `https://acp.copernicus.org/articles/21/13207/2021/`

Hersbach, H., B. Bell, P. Berrisford, S. Hirahara, A. Horányi, J. Muñoz-Sabater, J. Nicolas, C. Peubey, R. Radu, D. Schepers, A. Simmons, C. Soci, S. Abdalla, X. Abellan, G. Balsamo, P. Bechtold, G. Biavati, J. Bidlot, M. Bonavita, G. De Chiara, P. Dahlgren, D. Dee, M. Diamantakis, R. Dragani, J. Flemming, R. Forbes, M. Fuentes, A. Geer, L. Haimberger, S. Healy, R. J. Hogan, E. Hólm, M. Janisková, S. Keeley, P. Laloyaux, P. Lopez, C. Lupu, G. Radnoti, P. De Rosnay, I. Rozum, F. Vamborg, S. Villaume, and J. Thépaut, 2020: The ERA5 global reanalysis. *Quarterly Journal of the Royal Meteorological Society*, **146**, 1999–2049, doi:10.1002/qj.3803.
URL `https://rmets.onlinelibrary.wiley.com/doi/10.1002/qj.3803`

Holton, J. R. and G. J. Hakim, 2013: *An Introduction to Dynamic Meteorology*. 5th ed. Academic Press.

Holtslag, A. A. M. and F. T. M. Nieuwstadt, 1986: Scaling the atmospheric boundary layer. *Boundary-Layer Meteorology*, **36**, 201–209, doi:10.1007/BF00117468.
URL `http://link.springer.com/10.1007/BF00117468`

Hong, S.-Y., Y. Noh, and J. Dudhia, 2006: A New Vertical Diffusion Package with an Explicit Treatment of Entrainment Processes. *Monthly Weather Review*, **134**, 2318–2341, doi:10.1175/MWR3199.1.
URL `http://journals.ametsoc.org/doi/10.1175/MWR3199.1`

Iacono, M. J., J. S. Delamere, E. J. Mlawer, M. W. Shephard, S. A. Clough, and W. D. Collins, 2008: Radiative forcing by long-lived greenhouse gases: Calculations with the AER radiative transfer models. *Journal of Geophysical Research: Atmospheres*, **113**, 2008JD009944, doi:10.1029/2008JD009944.

URL `https://agupubs.onlinelibrary.wiley.com/doi/10.1029/2008JD009944`

Kalthoff, N., M. Kohler, C. Barthlott, B. Adler, S. Mobbs, U. Corsmeier, K. Träumner, T. Foken, R. Eigenmann, L. Krauss, S. Khodayar, and P. Di Girolamo, 2011: The dependence of convection-related parameters on surface and boundary-layer conditions over complex terrain. *Quarterly Journal of the Royal Meteorological Society*, **137**, 70–80, doi:10.1002/qj.686.

URL `https://rmets.onlinelibrary.wiley.com/doi/10.1002/qj.686`

Knuteson, R. O., H. E. Revercomb, F. A. Best, N. C. Ciganovich, R. G. Dedecker, T. P. Dirkx, S. C. Ellington, W. F. Feltz, R. K. Garcia, H. B. Howell, W. L. Smith, J. F. Short, and D. C. Tobin, 2004: Atmospheric Emitted Radiance Interferometer. Part I: Instrument Design. *Journal of Atmospheric and Oceanic Technology*, **21**, 1763–1776, doi:10.1175/JTECH-1662.1.

URL `http://journals.ametsoc.org/doi/10.1175/JTECH-1662.1`

Kustas, W. P. and W. Brutsaert, 1987: Virtual heat entrainment in the mixed layer over very rough terrain. *Boundary-Layer Meteorology*, **38**, 141–157, doi:10.1007/BF00121561.

URL `http://link.springer.com/10.1007/BF00121561`

Lapworth, A., 2006: The Morning Transition of the Nocturnal Boundary Layer. *Boundary-Layer Meteorology*, **119**, 501–526, doi:10.1007/s10546-005-9046-0.

URL `http://link.springer.com/10.1007/s10546-005-9046-0`

Lee, T. R. and S. F. J. De Wekker, 2016: Estimating Daytime Planetary Boundary Layer Heights over a Valley from Rawinsonde Observations at a Nearby Airport: An Application to the Page Valley in Virginia, United States. *Journal of Applied Meteorology and Climatology*, **55**, 791–809, doi:10.1175/JAMC-D-15-0300.1. URL `https://journals.ametsoc.org/view/journals/apme/55/3/jamc-d-15-0300.1.xml`

LeMone, M. A., W. M. Angevine, C. S. Bretherton, F. Chen, J. Dudhia, E. Fedorovich, K. B. Katsaros, D. H. Lenschow, L. Mahrt, E. G. Patton, J. Sun, M. Tjernström, and J. Weil, 2019: 100 Years of Progress in Boundary Layer Meteorology. *Meteorological Monographs*, **59**, 9.1–9.85, doi:10.1175/AMSMONOGRAPHS-D-18-0013.1. URL `http://journals.ametsoc.org/doi/10.1175/AMSMONOGRAPHS-D-18-0013.1`

Lenschow, D. H., P. B. Krummel, and S. T. Siems, 1999: Measuring Entrainment, Divergence, and Vorticity on the Mesoscale from Aircraft. *Journal of Atmospheric and Oceanic Technology*, **16**, 1384–1400, doi:10.1175/1520-0426(1999)016¡1384:MEDAVO¿2.0.CO;2. URL `http://journals.ametsoc.org/doi/10.1175/1520-0426(1999)016<1384:MEDAVO>2.0.CO;2`

Liu, F., F. Yi, Z. Yin, Y. Zhang, Y. He, and Y. Yi, 2021: Measurement report: characteristics of clear-day convective boundary layer and associated entrainment zone as observed by a ground-based polarization lidar over Wuhan (30.5° N, 114.4° E). *Atmospheric Chemistry and Physics*, **21**, 2981–2998, doi:10.5194/acp-21-2981-2021.

URL `https://acp.copernicus.org/articles/21/2981/2021/`

Mahrt, L., R. C. Heald, D. H. Lenschow, B. B. Stankov, and I. Troen, 1979: An observational study of the structure of the nocturnal boundary layer. *Boundary-Layer Meteorology*, **17**, 247–264, doi:10.1007/BF00117983.

URL `http://link.springer.com/10.1007/BF00117983`

Miralles, D. G., A. J. Teuling, C. C. Van Heerwaarden, and J. Vilà-Guerau De Arellano, 2014: Mega-heatwave temperatures due to combined soil desiccation and atmospheric heat accumulation. *Nature Geoscience*, **7**, 345–349, doi:10.1038/ngeo2141.

URL `https://www.nature.com/articles/ngeo2141`

Mlawer, E. J., S. J. Taubman, P. D. Brown, M. J. Iacono, and S. A. Clough, 1997: Radiative transfer for inhomogeneous atmospheres: RRTM, a validated correlated-k model for the longwave. *Journal of Geophysical Research: Atmospheres*, **102**, 16663–16682, doi:10.1029/97JD00237.

URL `https://agupubs.onlinelibrary.wiley.com/doi/10.1029/97JD00237`

Nelson, E., R. Stull, and E. Eloranta, 1989: A Prognostic Relationship for Entrainment Zone Thickness. *Journal of Applied Meteorology*, **28**, 885–903, doi:10.1175/1520-0450(1989)028¡0885:APRFEZ¿2.0.CO;2.

URL `http://journals.ametsoc.org/doi/10.1175/1520-0450(1989)028<0885:APRFEZ>2.0.CO;2`

Newsom, R. K. and R. Krishnamurthy, 2022: Doppler Lidar (DL) Instrument Handbook. Technical report, U.S. Department of Energy, Atmospheric Radiation Measurement user facility, Richland, Washington. DOE/SC-ARM-TR-101.

Nielsen, K. F. and D. A. Rahn, 2022: Morning Transition of the Boundary Layer over Dallas–Fort Worth. *Journal of Applied Meteorology and Climatology*, **61**, 1433–1448, doi:10.1175/JAMC-D-21-0169.1.
URL `https://journals.ametsoc.org/view/journals/apme/61/10/JAMC-D-21-0169.1.xml`

Otte, M. J. and J. C. Wyngaard, 2001: Stably Stratified Interfacial-Layer Turbulence from Large-Eddy Simulation. *Journal of the Atmospheric Sciences*, **58**, 3424–3442, doi:10.1175/1520-0469(2001)058¡3424:SSILTF¿2.0.CO;2.
URL `http://journals.ametsoc.org/doi/10.1175/1520-0469(2001)058<3424:SSILTF>2.0.CO;2`

Pal, S., A. Behrendt, and V. Wulfmeyer, 2010: Elastic-backscatter-lidar-based characterization of the convective boundary layer and investigation of related statistics. *Annales Geophysicae*, **28**, 825–847, doi:10.5194/angeo-28-825-2010.
URL `https://angeo.copernicus.org/articles/28/825/2010/`

Peters-Lidard, C. D. and L. H. Davis, 2000: Regional Flux Estimation in a Convective Boundary Layer Using a Conservation Approach. *Journal of Hydrometeorology*, **1**, 170–182, doi:10.1175/1525-7541(2000)001¡0170:RFEIAC¿2.0.CO;2.

URL `http://journals.ametsoc.org/doi/10.1175/1525-7541(2000)001<0170:RFEIAC>2.0.CO;2`

Ropelewski, C. F. and M. S. Halpert, 1986: North American Precipitation and Temperature Patterns Associated with the El Niño/Southern Oscillation (ENSO). *Monthly Weather Review*, **114**, 2352–2362, doi:10.1175/1520-0493(1986)114¡2352:NAPATP¿2.0.CO;2.

URL `http://journals.ametsoc.org/doi/10.1175/1520-0493(1986)114<2352:NAPATP>2.0.CO;2`

Rosenberger, T. E., T. Heus, G. N. Raghunathan, D. D. Turner, T. J. Wagner, and J. M. Simonson, 2025: A large-eddy simulation exploration of the assumptions used in retrieving entrainment from a mixing diagram approach with ground-based remote sensors. *Atmospheric Measurement Techniques*, **18**, 5129–5140, doi:10.5194/amt-18-5129-2025.

URL `https://amt.copernicus.org/articles/18/5129/2025/`

Santanello, J. A., P. A. Dirmeyer, C. R. Ferguson, K. L. Findell, A. B. Tawfik, A. Berg, M. Ek, P. Gentine, B. P. Guillod, C. Van Heerwaarden, J. Roundy, and V. Wulfmeyer, 2018: Land–Atmosphere Interactions: The LoCo Perspective. *Bulletin of the American Meteorological Society*, **99**, 1253–1272, doi:10.1175/BAMS-D-17-0001.1.

URL `https://journals.ametsoc.org/view/journals/bams/99/6/bams-d-17-0001.1.xml`

Santanello, J. A., M. A. Friedl, and W. P. Kustas, 2005: An Empirical Investigation of Convective Planetary Boundary Layer Evolution and Its Relationship with the Land Surface. *Journal of Applied Meteorology*, **44**, 917–932, doi:10.1175/JAM2240.1. URL `https://journals.ametsoc.org/doi/10.1175/JAM2240.1`

Santanello, J. A., C. D. Peters-Lidard, and S. V. Kumar, 2011: Diagnosing the Sensitivity of Local Land–Atmosphere Coupling via the Soil Moisture–Boundary Layer Interaction. *Journal of Hydrometeorology*, **12**, 766–786, doi:10.1175/JHM-D-10-05014.1. URL `https://journals.ametsoc.org/view/journals/hydr/12/5/jhm-d-10-05014_1.xml`

Santanello, J. A., C. D. Peters-Lidard, S. V. Kumar, C. Alonge, and W.-K. Tao, 2009: A Modeling and Observational Framework for Diagnosing Local Land–Atmosphere Coupling on Diurnal Time Scales. *Journal of Hydrometeorology*, **10**, 577–599, doi:10.1175/2009JHM1066.1. URL `http://journals.ametsoc.org/doi/10.1175/2009JHM1066.1`

Schumacher, D. L., J. Keune, C. C. Van Heerwaarden, J. Vilà-Guerau De Arellano, A. J. Teuling, and D. G. Miralles, 2019: Amplification of mega-heatwaves through heat torrents fuelled by upwind drought. *Nature Geoscience*, **12**, 712–717, doi:10.1038/s41561-019-0431-6. URL `https://www.nature.com/articles/s41561-019-0431-6`

Seibert, P., 2000: Review and intercomparison of operational methods for the determination of the mixing height. *Atmospheric Environment*, **34**, 1001–1027, doi:10.1016/S1352-2310(99)00349-0.

URL `https://linkinghub.elsevier.com/retrieve/pii/S1352231099003490`

Seidel, D. J., Y. Zhang, A. Beljaars, J. Golaz, A. R. Jacobson, and B. Medeiros, 2012: Climatology of the planetary boundary layer over the continental United States and Europe. *Journal of Geophysical Research: Atmospheres*, **117**, 2012JD018143, doi:10.1029/2012JD018143.

URL `https://agupubs.onlinelibrary.wiley.com/doi/10.1029/2012JD018143`

Sorbjan, Z., 1996: Effects Caused by Varying the Strength of the Capping Inversion Based on a Large Eddy Simulation Model of the Shear-Free Convective Boundary Layer. *Journal of the Atmospheric Sciences*, **53**, 2015–2024, doi:10.1175/1520-0469(1996)053¡2015:ECBVTS¿2.0.CO;2.

URL `http://journals.ametsoc.org/doi/10.1175/1520-0469(1996)053<2015:ECBVTS>2.0.CO;2`

Stouffer, B. C., D. J. Stensrud, C. L. Comer, Y. Zhang, and M. R. Kumjian, 2024: An Investigation of Convective Boundary Layer Depth and Entrainment Zone Properties Using Dual-Polarization Radar and Balloon-Borne Observations. *Journal of Atmospheric and Oceanic Technology*, **41**, 1213–1228, doi:10.1175/JTECH-D-23-0165.1.

URL `https://journals.ametsoc.org/view/journals/atot/41/12/JTECH-D-23-0165.1.xml`

Stouffer, B. C., D. J. Stensrud, and Y. Zhang, 2025: Estimates of Entrainment Zone Depth across the United States from Dual-Polarization WSR-88D Radar Observations.

Monthly Weather Review, **153**, 2829–2843, doi:10.1175/MWR-D-25-0146.1.
URL `https://journals.ametsoc.org/view/journals/mwre/153/12/MWR-D-25-0146.1.xml`

Stull, R. B., 1988: *An Introduction to Boundary Layer Meteorology*. Springer, Dordrecht, Netherlands.

Sullivan, P. P., C.-H. Moeng, B. Stevens, D. H. Lenschow, and S. D. Mayor, 1998: Structure of the Entrainment Zone Capping the Convective Atmospheric Boundary Layer. *Journal of the Atmospheric Sciences*, **55**, 3042–3064, doi:10.1175/1520-0469(1998)055¡3042:SOTEZC¿2.0.CO;2.
URL `http://journals.ametsoc.org/doi/10.1175/1520-0469(1998)055<3042:SOTEZC>2.0.CO;2`

Tang, S., S. Xie, M. Zhang, Q. Tang, Y. Zhang, S. A. Klein, D. R. Cook, and R. C. Sullivan, 2019: Differences in Eddy-Correlation and Energy-Balance Surface Turbulent Heat Flux Measurements and Their Impacts on the Large-Scale Forcing Fields at the ARM SGP Site. *Journal of Geophysical Research: Atmospheres*, **124**, 3301–3318, doi:10.1029/2018JD029689.
URL `https://agupubs.onlinelibrary.wiley.com/doi/10.1029/2018JD029689`

Tennekes, H., 1973: A Model for the Dynamics of the Inversion Above a Convective Boundary Layer. *Journal of the Atmospheric Sciences*, **30**, 558–567, doi:10.1175/1520-0469(1973)030¡0558:AMFTDO¿2.0.CO;2.

URL `http://journals.ametsoc.org/doi/10.1175/1520-0469(1973)030<0558:AMFTDO>2.0.CO;2`

Tennekes, H. and A. G. M. Driedonks, 1981: Basic entrainment equations for the atmospheric boundary layer. *Boundary-Layer Meteorology*, **20**, 515–531, doi:10.1007/BF00122299.
URL `http://link.springer.com/10.1007/BF00122299`

Turner, D. D. and W. G. Blumberg, 2019: Improvements to the AERIoe Thermodynamic Profile Retrieval Algorithm. *IEEE Journal of Selected Topics in Applied Earth Observations and Remote Sensing*, **12**, 1339–1354, doi:10.1109/JSTARS.2018.2874968.
URL `https://ieeexplore.ieee.org/document/8576572/`

Turner, D. D. and U. Löhnert, 2014: Information Content and Uncertainties in Thermodynamic Profiles and Liquid Cloud Properties Retrieved from the Ground-Based Atmospheric Emitted Radiance Interferometer (AERI). *Journal of Applied Meteorology and Climatology*, **53**, 752–771, doi:10.1175/JAMC-D-13-0126.1.
URL `https://journals.ametsoc.org/view/journals/apme/53/3/jamc-d-13-0126.1.xml`

Van Heerwaarden, C. C., J. Vilà-Guerau De Arellano, A. F. Moene, and A. A. M. Holtslag, 2009: Interactions between dry-air entrainment, surface evaporation and convective boundary-layer development. *Quarterly Journal of the Royal Meteorological Society*, **135**, 1277–1291, doi:10.1002/qj.431.
URL `https://rmets.onlinelibrary.wiley.com/doi/10.1002/qj.431`

Van Ulden, A. P. and J. Wieringa, 1996: Atmospheric boundary layer research at Cabauw. *Boundary-Layer Meteorology*, **78**, 39–69, doi:10.1007/BF00122486. URL `http://link.springer.com/10.1007/BF00122486`

vanZanten, M. C., P. G. Duynkerke, and J. W. M. Cuijpers, 1999: Entrainment Parameterization in Convective Boundary Layers. *Journal of the Atmospheric Sciences*, **56**, 813–828, doi:10.1175/1520-0469(1999)056¡0813:EPICBL¿2.0.CO;2. URL `http://journals.ametsoc.org/doi/10.1175/1520-0469(1999)056<0813:EPICBL>2.0.CO;2`

Von Engeln, A. and J. Teixeira, 2013: A Planetary Boundary Layer Height Climatology Derived from ECMWF Reanalysis Data. *Journal of Climate*, **26**, 6575–6590, doi:10.1175/JCLI-D-12-00385.1. URL `http://journals.ametsoc.org/doi/10.1175/JCLI-D-12-00385.1`

Wagner, T. J., D. D. Turner, T. Heus, and W. G. Blumberg, 2022: Observing Profiles of Derived Kinematic Field Quantities Using a Network of Profiling Sites. *Journal of Atmospheric and Oceanic Technology*, **39**, 335–351, doi:10.1175/JTECH-D-21-0061.1. URL `https://journals.ametsoc.org/view/journals/atot/39/3/JTECH-D-21-0061.1.xml`

Wakefield, R. A., J. B. Basara, J. C. Furtado, B. G. Illston, C. R. Ferguson, and P. M. Klein, 2019: A Modified Framework for Quantifying Land–Atmosphere Covariability during Hydrometeorological and Soil Wetness Extremes in Oklahoma. *Journal of Applied Meteorology and Climatology*, **58**, 1465–1483, doi:10.1175/JAMC-D-18-0230.1.

URL `https://journals.ametsoc.org/view/journals/apme/58/7/jamc-d-18-0230.1.xml`

Wakefield, R. A., J. B. Basara, J. M. Shepherd, N. Brauer, J. C. Furtado, J. A. Santanello, and R. Edwards, 2021a: The Inland Maintenance and Reintensification of Tropical Storm Bill (2015) Part 1: Contributions of the Brown Ocean Effect. *Journal of Hydrometeorology*, doi:10.1175/JHM-D-20-0150.1.
URL `https://journals.ametsoc.org/view/journals/hydr/aop/JHM-D-20-0150.1/JHM-D-20-0150.1.xml`

Wakefield, R. A., D. D. Turner, and J. B. Basara, 2021b: Evaluation of a land-atmosphere coupling metric computed from a ground-based infrared interferometer. *Journal of Hydrometeorology*, doi:10.1175/JHM-D-20-0303.1.
URL `https://journals.ametsoc.org/view/journals/hydr/aop/JHM-D-20-0303.1/JHM-D-20-0303.1.xml`

Wakefield, R. A., D. D. Turner, T. Rosenberger, T. Heus, T. J. Wagner, J. Santanello, and J. Basara, 2023: A Methodology for Estimating the Energy and Moisture Budget of the Convective Boundary Layer Using Continuous Ground-Based Infrared Spectrometer Observations. *Journal of Applied Meteorology and Climatology*, **62**, 901–914, doi:10.1175/JAMC-D-22-0163.1.
URL `https://journals.ametsoc.org/view/journals/apme/62/7/JAMC-D-22-0163.1.xml`

Wilczak, J. M., E. E. Gossard, W. D. Neff, and W. L. Eberhard, 1996: Ground-based remote sensing of the atmospheric boundary layer: 25 years of progress. *Boundary-Layer Meteorology*, **78**, 321–349, doi:10.1007/BF00120940.
URL `http://link.springer.com/10.1007/BF00120940`

Wulfmeyer, V., 1999: Investigation of Turbulent Processes in the Lower Troposphere with Water Vapor DIAL and Radar–RASS. *Journal of the Atmospheric Sciences*, **56**, 1055–1076, doi:10.1175/1520-0469(1999)056¡1055:IOTPIT¿2.0.CO;2.
URL `http://journals.ametsoc.org/doi/10.1175/1520-0469(1999)056<1055:IOTPIT>2.0.CO;2`

Wulfmeyer, V., S. K. Muppa, A. Behrendt, E. Hammann, F. Späth, Z. Sorbjan, D. D. Turner, and R. M. Hardesty, 2016: Determination of Convective Boundary Layer Entrainment Fluxes, Dissipation Rates, and the Molecular Destruction of Variances: Theoretical Description and a Strategy for Its Confirmation with a Novel Lidar System Synergy. *Journal of the Atmospheric Sciences*, **73**, 667–692, doi:10.1175/JAS-D-14-0392.1.
URL `https://journals.ametsoc.org/view/journals/atsc/73/2/jas-d-14-0392.1.xml`

Wulfmeyer, V., D. D. Turner, B. Baker, R. Banta, A. Behrendt, T. Bonin, W. A. Brewer, M. Buban, A. Choukulkar, E. Dumas, R. M. Hardesty, T. Heus, J. Ingwersen, D. Lange, T. R. Lee, S. Metzendorf, S. K. Muppa, T. Meyers, R. Newsom, M. Osman, S. Raasch, J. Santanello, C. Senff, F. Späth, T. Wagner, and T. Weckwerth, 2018: A New Research

Approach for Observing and Characterizing Land–Atmosphere Feedback. *Bulletin of the American Meteorological Society*, **99**, 1639–1667, doi:10.1175/BAMS-D-17-0009.1. URL `https://journals.ametsoc.org/view/journals/bams/99/8/bams-d-17-0009.1.xml`

Yamada, T. and S. Berman, 1979: A Critical Evaluation of a Simple Mixed-Layer Model with Penetrative Convection. *Journal of Applied Meteorology*, **18**, 781–786, doi:10.1175/1520-0450(1979)018¡0781:ACEOAS¿2.0.CO;2. URL `http://journals.ametsoc.org/doi/10.1175/1520-0450(1979)018<0781:ACEOAS>2.0.CO;2`